POLITECNICO DI MILANO

School of Industrial and Information Engineering

Master of Science in MECHANICAL ENGINEERING

Vibration damping and cyclic loading behavior of aluminum foam filled tubes

Supervisors:
Prof. Matteo Strano
Prof. Philippe Bocher (ÉTS Montréal)

M.Sc. Thesis of :
Alessandro MARRA

ACADEMIC YEAR 2013/2014

Contents

List of Figures

List of Tables

Abstract

Among the scientific and industrial realities, metal foams are unanimously considered as interesting and competitive materials. Indeed, thanks to their porous structure, these innovative materials can boast of having very interesting mechanical and physical properties compared to bulk materials. Foam filling of hollow structures is a clever solution that confers improvements both in stiffness to weight ratio and absorption of energy to the host material, so that automotive and aerospace industry are progressively making use of this solution.

The principal aim of this work is investigating on the damping properties and the cyclic loading behavior of foam filled titanium tubes. In order to determine the influence of these factors in damping capacity, tubes with two level of density in foam and two kind of interface (natural and bonded) between tube and foam will be studied. A modal analysis due to impact excitation will be performed on each tube, mainly to investigate the damping. Furthermore, displacement, energy and acoustic emission (AE) evolution during cyclic bending loading will be monitored and investigated. Finally, a comparison between the two kind of interfaces in both the damping and fatigue behavior will be proposed.

In addition to this, a vibration test will be designed and performed on foam filled steel tubes, in order to question the damping capacity of foam filling at 30 Hz. A structure designed to vibrate at this frequency will be excited and the damping computed through a modal analysis. This topic has been pushed by the interest of *Bell Textron Canada* in making use of foam-filled tubes as structural components in helicopters whose rotor excitations' frequency are indeed close to 30 Hz. By the way, the whole study has been developed in partnership between *Politecnico di Milano*, *MUSP* laboratory of Piacenza and *ÉTS (École de technologie Superiéure)* of Montréal.

Keywords: metal foam filling, structural vibrations damping, three point bending, fatigue behavior, acoustic emissions, helicopters and machine tools components.

Chapter 1) Introduction on Metal foams

Metal Foams are innovative materials belonging to the family of Cellular Solids. Their peculiarity is the porous structure that allows them to have an excellent stiffness to weight ratio and many other interesting characteristics. The cell is the single unit that builds the assembly of the whole material. This unit is an open or closed junction of walls and edges surrounding the non-solid part of the material that can be vacuum, air or a gas depending on the production process. The result of this assembly is a low density non-homogeneous metal whose porosity opens several possibilities of applications in many fields.

1.1 Making Metal Foams

Despite metal foams are commonly considered as innovative materials, the first patent concerning metal foaming is dated at 1925 [1]. De Meller first described a process comprising the injection of an inert gas or the addition of a blowing agent, such as a carbonate, to a molten metal, during the melt stirring. In the following decades, many studies have been conducted all over the world (USA, Japan, Canada, Europe) in order to improve De Meller's patent, and many other processes have been developed. Nowadays making

metal foam is a relatively easy practice, customizable for almost any kind of needs and shapes.

1.1.1 Processes

During the last decades many studies on metal foaming have been developed, so that now there are nine distinct procedures of which five are established commercially. They may be grouped in four main classes: those in which the foam is formed from a vapor phase; those in which the foam is electrodeposited from an aqueous solution; those that depend on liquid state processing; those in which the foam is created in the solid state. Despite of the conceptual classification that helps understanding different ways of making foams, a brief description of all the nine production processes follows:

1) *Melt gas injection (air bubbling)*: a gas (typically air) is injected into molten Al-SiC or Al-Al_2O_3 alloys. Bubbles float to the melt surface, drain, and then begin to solidify until foam is obtained.

2) *Gas releasing particle decomposition in the melt*: calcium, to rise viscosity, and then TiH_2 (titanium hydride),as foaming agent, are added to molten aluminum. As soon as the TiH_2 particles are added, the melt is stirred and a foam forms above it. When foaming is complete, the melt is cooled to solidify the foam before the hydrogen escapes and the bubble coalesce or collapse.

3) *Gas releasing particles decomposition in semi-solids*: consolidation of a metal powder (commonly aluminum alloys) with a particulate foaming agent (TiH_2 again) followed by heating into the mushy state when the foaming agent releases hydrogen, expanding the materials. This process will be detailed in the paragraph 1.1.2.

4) *Casting using a polymer or wax precursor as template*: a ceramic mold is manufactured from a wax or polymer-foam precursor. The precursor is then burned out and molten metal

or metal powder slurry (sintered later) is infiltrated into the mold. This process allows the casting of several kind of metals, even stainless steel.

5) *Metal deposition on cellular preforms*: Vapor phase deposition (CVD process) or electro-deposition of metal (typically Ni or Ti) onto a polymer foams that is subsequently burned out, leaving cell edges with hollow cores. A subsequent sintering step is used to densify the ligaments.

6) *Entrapped gas expansion*: High-pressure inert gas is trapped in pores by powder hot isostatic pressing (HIPing), followed by the expansion of the gas at elevated temperature. Boeing used this process to create low-density core Ti-6Al-4V sandwich panels.

7) *Hollow spheres structures*: Sintering of hollow spheres. The spheres are made by an inert gas atomization process, or from metal-oxide or hybrid spheres followed by reduction or dehydration, or by vapor-deposition of metal onto polymer spheres.

8) *Co-compaction or casting of two materials, one leachable*: a metal powder (Al powder) and a leachable one (e.g. salt) are mixed and compressed. The structure is then leached to leave a metal foam skeleton.

9) *Gas-metal eutectic solidification:* An alloy, exhibiting a eutectic, is melted, saturated with hydrogen under pressure, and then directionally solidified, progressively reducing the pressure. During solidification, solid metal and hydrogen simultaneously form by a gas eutectic reaction, resulting in a porous material containing hydrogen-filled pores.

The first five of these are in commercial production. Each method is able to produce a small subset of metals to create a porous material with a limited range of relative density (ρ/ρ_s), and cell sizes. Figure 1.1 shows each process, and the related product's cell type, in a cell size-relative density diagram. It is possible to remark that the trend is inversely proportional so

that the cell size grows as the relative density decreases. Moreover, it is hard to obtain an open cell structure with high relative density (except for mold casting).

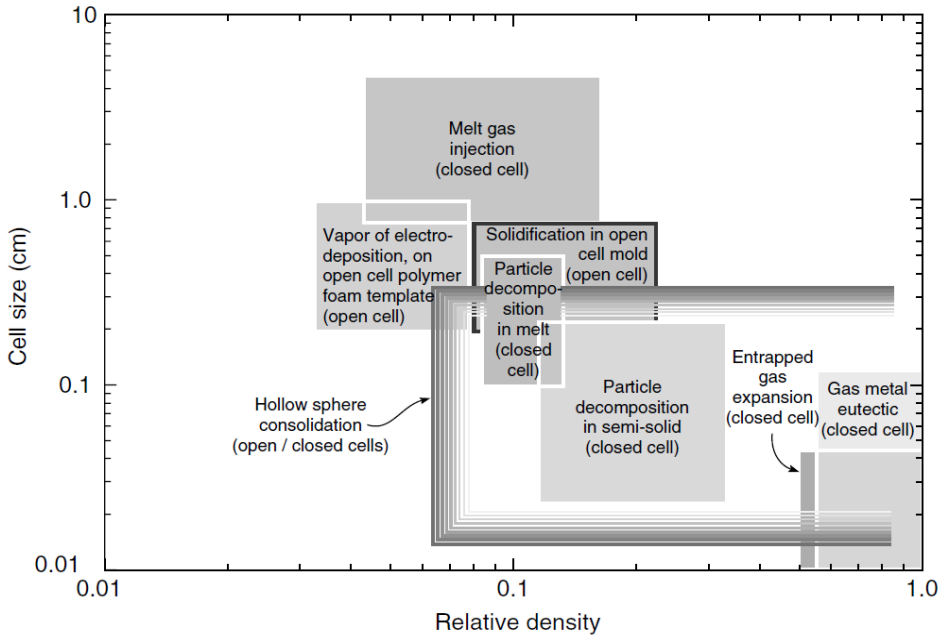

Figure 1.1: Diagram showing production methods related to the characteristics of the foam produced [2]

1.1.2 Gas releasing particles decomposition in semi-solids (Alulight precursors)

This is the method used to produce the aluminum foam filling the tubes studied in this work. As previously mentioned, a crucial part of this method is making the precursors for foaming. These are the result of mixing and compacting a foaming agent and metal powder. Titanium hydride begins to decompose, releasing hydrogen, at about 465°C, and this is compatible with aluminum foaming since the melting point of aluminum's alloys is at about 660°C. The precursors' manufacturing sequence is in Figure 1.2.a. It begins by combining particles of a foaming agent with an aluminum alloy powder in a mixer (if metal hydrides are used, a content of less 1% is sufficient in

most cases). After the ingredients are mixed, the powder is compacted and then extruded into a bar or plate. The extrusion process can be axial (Figure 1.2.b) or centrifugal (Figure 1.2.c).

Unfortunately, no machines like these are present in our laboratory. Because of this, we ask to Alulight to supply us the precursors. The process they use to make the precursors consists in inserting the mixture of aluminum powder and TiH2 in a rotational machine that forces it into a die (Figure 1.2.c). Once passed the die, the mixture is compact and cut into bars or disks. The characteristics of the bars are in Table 1.1.

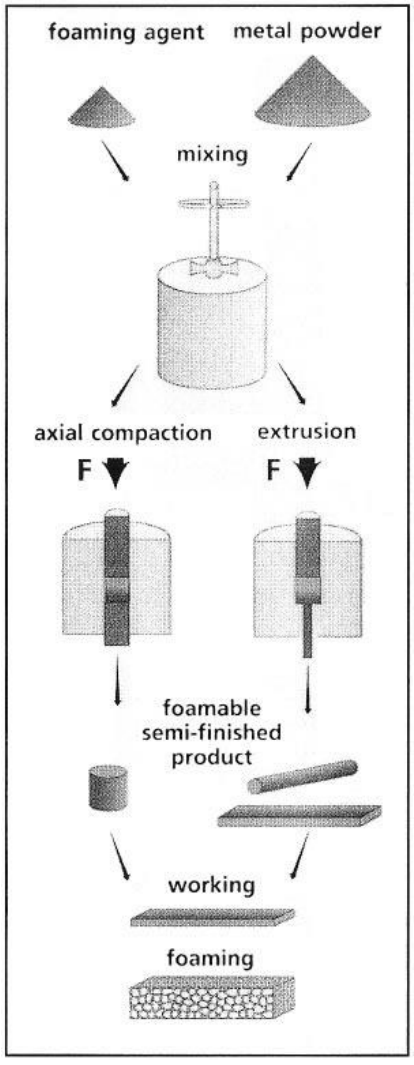

a)

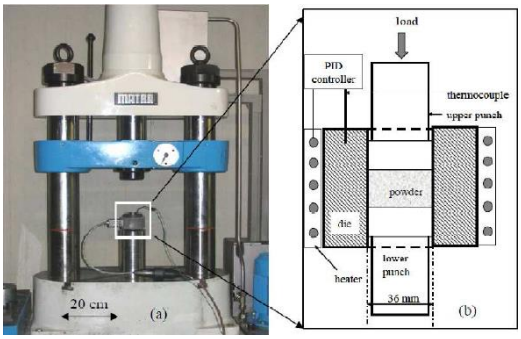

b)

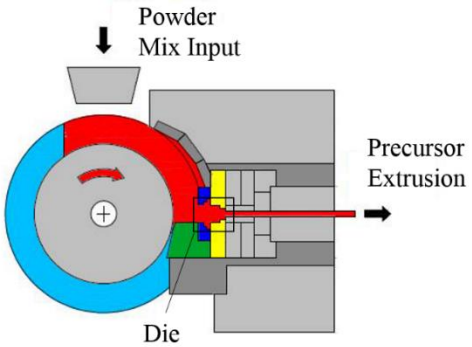

c)

Figure 1.2: a) Precursors manufacturing and foaming [3]; b) Hot pressing precursors [4]; c) Continuous rotating extrusion for Alulight precursors

Figure 1.3: Alulight precursors

Type	Diameter	Metal Powder	Foaming Agent	Linear Density
Bar	22mm	AlMg1Si0.6 (99.2%)	TiH2 (0.8%)	0.227 g/mm

Table 1.1: Characteristics of Alulight precursors

Once the precursors are ready, the foaming process takes place (Figure 1.4.a). The bars or disks are placed into a mold (see an example of the mold used for our specimens in Figure 1.4.b), and then this one into an oven. The temperature slowly rises up to a little above the solidus temperature of the aluminum alloy. This is to ensure that the titanium hydride decomposes releasing hydrogen whit a high internal pressure and, at the same time, the bubbles does not collapse cause of the viscosity of the metal, not completely molten. The bubbles expand by semi-solid flow and the aluminum swells, creating a foam that fills the mold. The process gives components with the same shape of the container. The foam has closed cells with diameters that range from 1mm to 5mm.

a) *b)*

Figure 1.4: Foaming in the mold [2]; b) Alulight precursors in mold

IFAM, Bremen [2], have developed a variant of the process in which panel structures are made by first roll-bonding aluminum of steel face-sheets onto a core-sheet of unexpanded precursors. This unexpanded structure is then pressed or deep-drawn to shape and placed in a furnace to expand the cores, giving a shaped, metal foam cored sandwich-panel. Only foamed aluminum is commercially available today, but other alloys foams are being developed using different foaming agents.

1.2 Properties of Foams

The reason why recently metal foams are object of several studies stands in the interesting properties characterizing them. However, metal foams are still inadequately characterized. This is due to the strong non-homogeneity, anisotropy and defects, by which we mean wiggly, buckled or broken cell walls, and cells of exceptional size or shape. Anyway, the picture is changing rapidly and the producers of metal foams have aggressive development programs for their materials. This paragraph aims at giving a brief description

of general properties of metal foams focusing on the ones that are topics of this study.

1.2.1 Overview on mechanical and physical properties

Unlike bulk materials, several factors influence metal foams' properties. It is possible to identify at least three main parameters of influence, such as:

- Metal they are made of;
- Structure: *open*, *closed* or in the middle;
- Relative density ρ/ρ_s where ρ and ρ_s are the densities of the bulk material and the foam respectively

A definition of the open or closed structure is required. There is an *open* structure when a fluid is able to pass through each cell inside the foam; this means that each cell is communicating and that there is no gas or air trapped inside. On the other hand we have a *closed* structure when each cell is a sort of closed box, isolated each other and there is no possibility for a fluid to pass through.

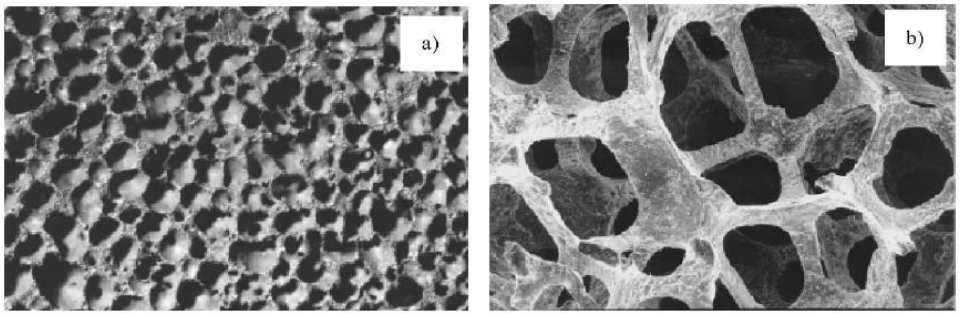

Figure 1.5: a) Closed vs b) open cell structure [5]

However, the most of metal foams commercially available are not completely open or closed but they are in between those two extremes. This is due to the randomness of the structure consequent to the inability of most production processes to form equally shaped bubbles or cells.

There are three main suppliers for metal foams: Cymat, Mepura (Alulight) and Shinko (Alporas). Cymat uses 'Melt gas injection' (see paragraph 1.1.1) to produce an Al-SiC foam with a relative density ρ/ρ_s between 0.02 and 0.2 and an average cell size approaching 5 mm. Shinko Wire Co. Ltd. has developed the Alporas process (see 'Gas releasing particle decomposition in the melt' in paragraph 1.1.1) obtaining a foam with smaller cells and relative density between 0.08 and 0.2. Mepura instead uses the 'Gas releasing particles decomposition in semi-solids' method whit Alulight precursors to produce a foam with even smaller cells, and relative density between 0.1 and 0.35. An example of the foams produced by these suppliers is in Figure 1.6: the difference in cell size is connected to a difference in relative density.

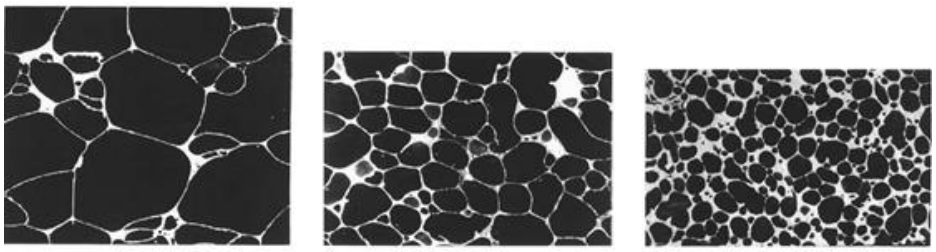

a) *b)* *c)*

Figure 1.6: a) Cymat with ρ/ρs =0.05; b) Shinko with ρ/ρs =0.09; c) Mepura with ρ/ρs =0.25 [2]

There are many other suppliers and many other type of metal foams, however these three are the most common and they give an example of different points in the wide spectrum of metal foams.

As a rule of thumb, there is a scaling relation for the most of the properties of metal foams that relates the general property *P** of the foam to the general property P_s of the related bulk material through the relative

density ρ/ρ_s and other constant coefficients like α and n. The relation take the form:

$$\frac{P^*}{P_s} = \alpha \left(\frac{\rho}{\rho_s}\right)^n$$

Mechanical properties

The mechanical behavior of metal foams differs from bulk materials, especially for compression mode. Figure 1.7.a shows a schematic stress-strain curve for compression: initial loading appears to be elastic but the curve is not straight, and its slope is less than the true modulus, because some cells yield at very low loads. The modulus E should be measured dynamically or from the unloading slope. Young's modulus E, shear modulus G and Poisson's ratio scale with density as:

$$E = \alpha_2 E_s \left(\frac{\rho}{\rho_s}\right)^n \qquad G = \alpha_2 G_s \left(\frac{\rho}{\rho_s}\right)^n \qquad \nu \approx 0.3$$

where n has a value between 1.8 and 2.2 and α_2 between 0.1 and 4 (they depend on the structure of the foam). For design purposes, it is helpful to know that, for metal foams, the tensile modulus is not the same as in compression; the tensile is greater, typically 10%. Moreover, anisotropy of cell shape can lead to significant differences between moduli in different directions.

A crucial characteristic of metal foam is the long and well-defined plateau stress σ_{pl}, visible in Figure 1.7.a. During this phase most of the plastic deformation takes place because the cell edges are yielding in bending. Closed-cell foams show a more complicated behavior: the stress rises with increasing strain because the cell faces carry membrane (tensile) stress. The plateau continues up to the densification strain, ε_D, beyond which the structure compacts and the stress rises steeply. Even the plateau stress σ_{pl}, and the densification strain, ε_D scale with density as:

$$\sigma_{pl} \approx (0.25 \div 0.35)\sigma_{y,s} \left(\frac{\rho}{\rho_s}\right)^m \qquad \varepsilon_D \approx \left(1 - \alpha_1 \frac{\rho}{\rho_s}\right)$$

Where m lies between 1.5 and 2.0 and α_1 between 1.4 and 2. These properties are important in energy-absorption that is the primary application

for metal foams nowadays. Indeed, the ability of showing a constant level of stress in a large strain range is much appreciated in crash absorption.

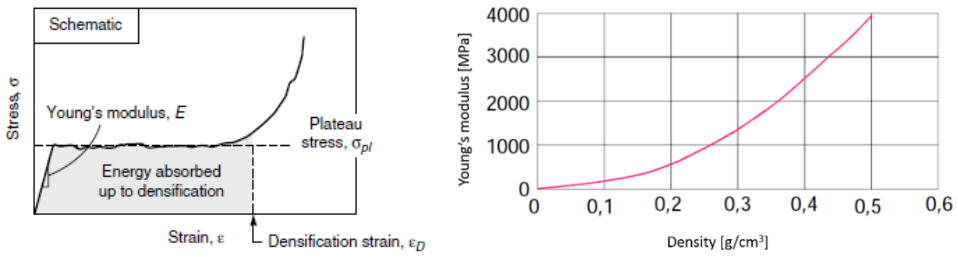

a) *b)*

Figure 1.7: a) Schematic compression behavior b) Young modulus vs density

The tensile stress-strain behavior of metal foams differs from the one in compression (see Figure 1.8). The slope of the curve before general yield is less than the real Young's modulus, implying considerable micro-plasticity even at very small strains. Beyond yield, metal foams harden up to the ultimate tensile strength beyond which they fall at a tensile ductility.

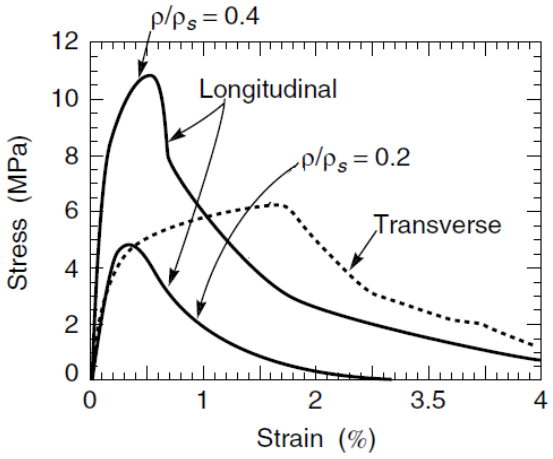

Figure 1.8: Tensile behavior for Alulight foams

Thermal properties

The melting point, specific heat and expansion coefficient of metal foams are the same as those of the metal from which they are made of. The thermal conductivity λ scales with density approximately as:

$$\lambda = \lambda_s \left(\frac{\rho}{\rho_s}\right)^q \qquad \text{with } q = 1.65 \div 1.8$$

Electrical properties

The only electrical property of interest is the resistivity, R. This scales with relative density approximately as:

$$R \approx R_s \left(\frac{\rho}{\rho_s}\right)^{-r} \qquad \text{with } r = 1.6 \div 1.85$$

1.2.2 Vibration damping and energy absorption

Unlike the other mechanical characteristics, surprisingly little attention is paid to mechanical damping of foams and other CMM (Cellular Metallic Materials). At the same time, foams are told to have a damping capacity corresponding to medium or even high damping materials according to existing classification [6]. If CMM are sometimes high damping materials, it is obvious that among the possible structural sources, their highly heterogeneous "composite" structure ("metal + gas") should be responsible. Moreover, it is well known that any kind of porosity enhances damping due to stress concentration [7].

All materials dissipate some energy during cyclic deformation, through intrinsic material damping and hysteresis. Damping becomes important when a component is subject to input excitation at or near its resonant frequencies. If a material is loaded elastically to a stress σ_{max} it stores elastic strain energy per unit volume, U; in a complete loading cycle it dissipates ΔU (as shown in Figure 1.9), where:

$$U = \int_0^{\sigma_{max}} \sigma \mathrm{d}\varepsilon = \frac{1}{2}\frac{\sigma_{max}^2}{E} \qquad \text{and} \qquad \Delta U = \oint \sigma_{max} \mathrm{d}\varepsilon \qquad [2]$$

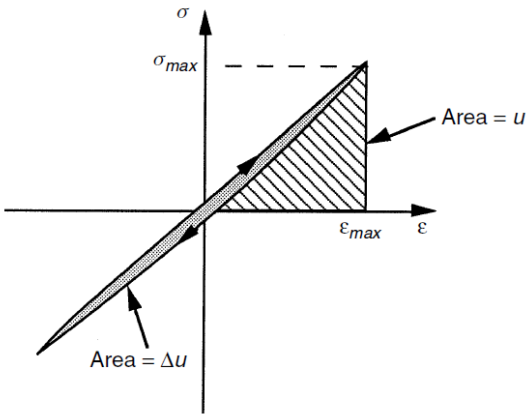

Figure 1.9: Hysteresis loop and energy dissipated in one loading cycle

There are several ways to characterize material damping, as well as several parameters to take into account. The loss coefficient η (or loss factor) is the energy loss per radian divided by the maximum elastic strain energy (or the total vibrational energy):

$$\eta = \frac{\Delta U}{2\pi U}$$

Other measures of damping include the proportional energy loss per cycle $D = \Delta U/U$, the damping ratio ζ, the logarithmic decrement δ, the loss angle ψ, and the quality factor Q. When damping is small ($\eta < 0.01$) and the system is excited near to resonance, these measures are related by

$$\eta = \frac{D}{2\pi} = 2\zeta = \frac{\delta}{\pi} = tan\,\psi = \frac{1}{Q} \qquad [2]$$

As a function of frequency, of amplitude and number of vibrations, and of the temperature, vibration damping depends both on the properties of the bulk material (composition, microstructure) and on the porous macrostructure, especially the value of porosity. Different internal friction mechanisms might be involved in damping in CMM: thermoelastic damping (Al, Zn foams), reversible dislocation motion (all studied materials), magneto-mechanical damping (Ni sponges), micro and macro-plastic deformation, crack-induced damping (most of sintered metals). Theories and experiments have indicated that, for polyphase materials composed of heterogeneous or non-equilibrium phases (as metal foams), thermoelastic

damping and dislocation movement primarily induce the energy dissipation. Thermoelastic damping can be described by the irreversible thermal flow induced under mechanical vibration. Defect or microstructural damping may be attributed to the reversible intrinsic movement of the microstructural defects under cyclic loading [8].

Many studies were carried out to identify the parameters that mostly influence damping and internal friction in metal foams. Golovin and Sinning [6] found the amplitude of vibration to be influent for both the reversible mechanism of movement of dislocation and the irreversible microplastic deformation and microcrack formation. In [7], Banhart studied the effect of density (and so porosity of the foam) and frequency on the loss factor of aluminum foams. He found that damping is stronger in foams with a lower density, because of the larger stress concentration in thinner membranes, and that the frequency of vibration does not seem to have a significant influence.

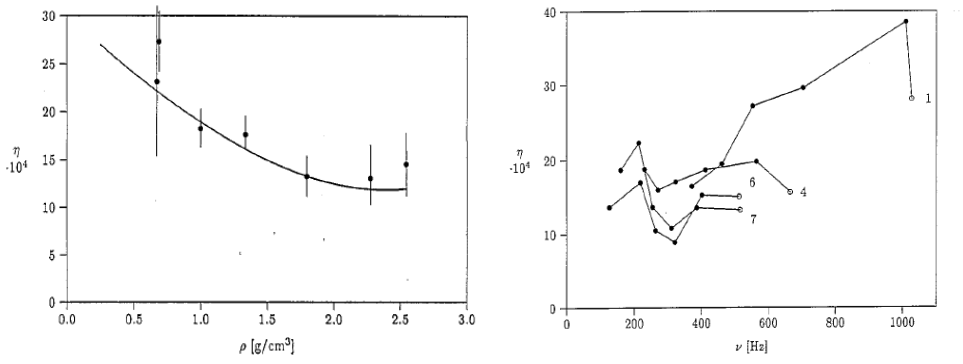

a) *b)*

Figure 1.10: a) Density and b) frequency influence on the loss factor for AlSi12 foam [7]

Always regarding frequency-dependent damping some found out that Al foams have no pronounced dependence from 100 to 1000 Hz, decrease with increasing frequency from 1 to 3 kHz and are damping-insensitive to frequencies between 0.04 and 4 Hz, even with significant deformation ($\varepsilon = 10^{-4}$) [6].

1.2.3 Fatigue behavior

In structural applications for metallic foams, such as in sandwich panels or filled tubes, it is necessary to take into account the degradation of strength with cyclic loading. A major cause of this degradation is the nucleation and growth of cracks. In a closed-cell foam, the cell faces are subject to membrane stresses while the cell edges bend predominantly. Consequently, crack initiation and growth occurs first in the cell faces and then progresses into the cell edges. When a metal foam is subjected to cyclic loading with an accompanying non-zero mean stress (Figure 1.11.a shows the stress behavior for this situation), the cell walls progressively bend under a compressive mean stress and progressively straighten under a tensile mean stress. This leads to a high macroscopic ductility in compression, and to brittle fracture in tension.

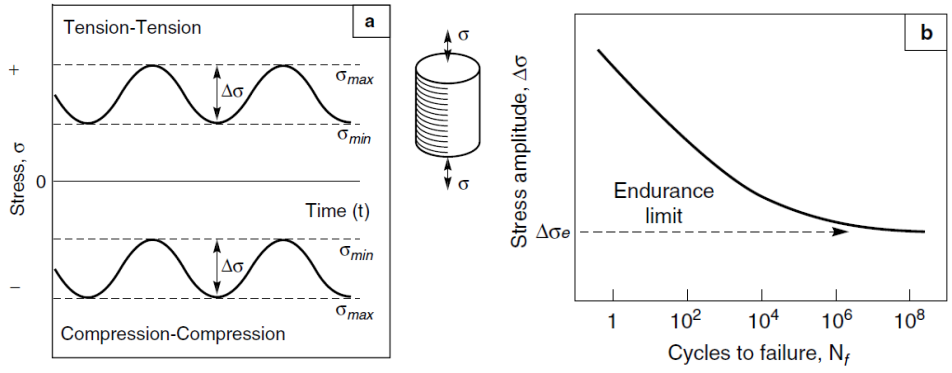

a) *b)*

Figure 1.11: a) Tension-tension and compression-compression load cycling b) definition of S-N curve

Figure 1.12.a and Figure 1.12.b show the S-N curves for Alporas and Alulight foams. The endurance limit is different for the compression-compression and tension-tension cyclic loading. This is due to the different behavior of this inhomogeneous material in compression and tension. The level of stress is often referred to the compression plateau stress σ_{pl} and, contrary to what is the habit for bulk materials, the fatigue life correlates well with the maximum stress of fatigue cycle σ_{max}, rather than the stress range $\Delta\sigma$.

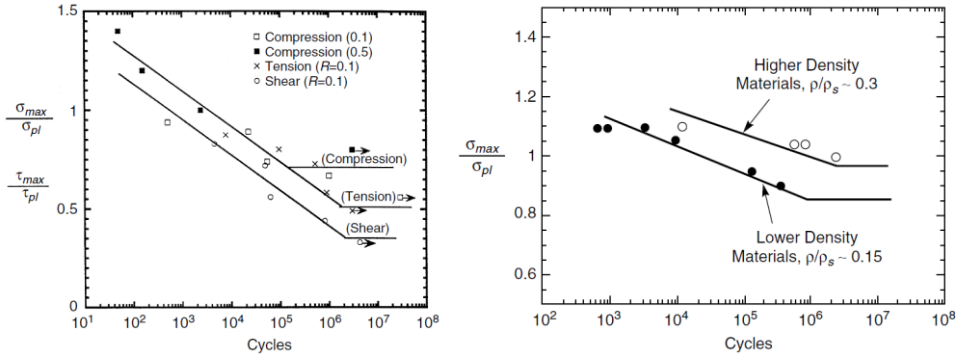

a) *b)*

Figure 1.12: a) S-N curves for compression-compression and tesnsion-tension fatigue of Alporas foam (relative density 0.11); b) S-N curves for compression-compression fatigue of Alulight foam (R=0.1) [2]

Figure 1.13 summarizes the fatigue strength for various aluminum foams by plotting the value of σ_{max} (normalized to the plateau stress) at a fatigue life of 10^7 cycles versus relative density, over a wide range of mean stresses. The fatigue strength of fully dense aluminum alloys has also been added: for tension–tension loading, with R = 0.1, the value of σ_{max} at the endurance limit is about 0.6 times the yield strength. It is interesting to notice how, when normalized to the uniaxial compressive strength, the fatigue strength of aluminum foams is comparable if not better than dense aluminum. Furthermore, no consistent trend with relative density is observed.

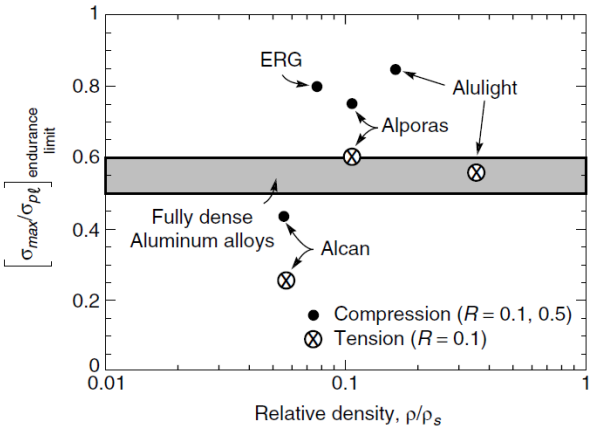

Figure 1.13: Endurance limit for compression and tension fatigue for different types of metal foams [2]

Fatigue-related instability of damping and Young Modulus

Cyclic loading is able to make changes in foams' micro and macrostructure such as to influence the damping properties of these materials. By instability we mean that internal friction measured in a preliminary test differs from the one measured in tests executed after cyclic loading. Golovin [9] studied the evolution of damping at different amplitudes and different number of cycles. He found that the energy absorbed for each loading cycle was growing with the number of cycles (Figure 1.14.a) and that the loss factor was growing with the amplitude of vibration and with the number of cycles as well (Figure 1.14.b).

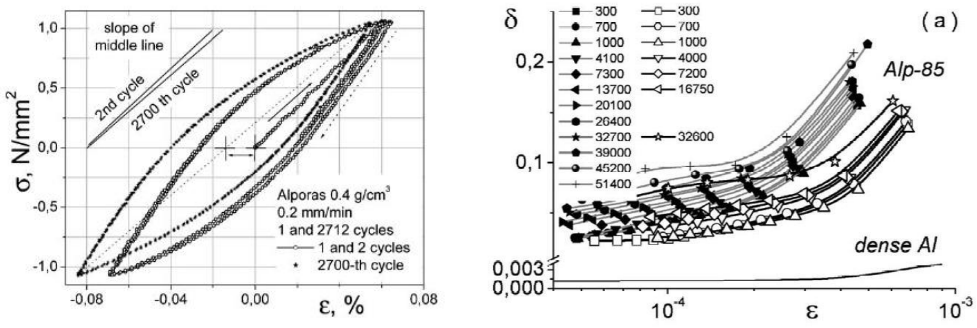

a) *b)*

Figure 1.14: a) Hysteresis loop showing the absorption of energy for cyclic loading and unloading b) loss factor as function of amplitude of vibration and number of cycles [9]

This evolution in energy absorption behavior was complementary to a decrease of the Young's modulus. This is a phenomenon noticeable even for bulk metallic materials. In CMM the concentration of stress in thin membranes enhances the crack initiation and propagation so that the accumulated damage (and energy) is visible even with lower levels of deformation.

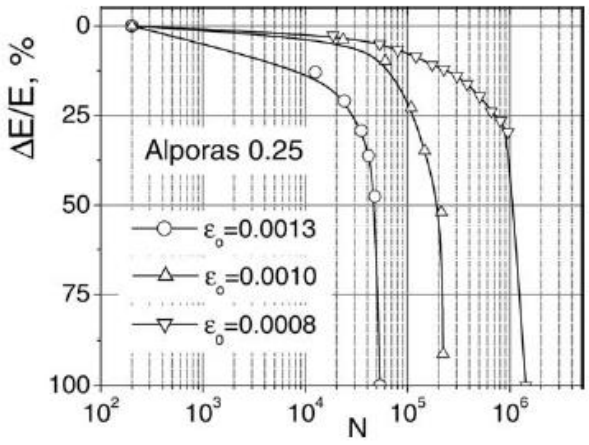

Figure 1.15: Elasticity modulus decrease during fatigue for different levels of ε

1.3 Peculiarities and related Applications

Metal foams have been finding several and new applications in the recent years. What really makes them interesting with respect to bulk materials is the possibility of playing on the morphology of the structure, shifting from open to close structure or adjusting the porosity according to the specific needs. Moreover, metal foams are easy shaping materials, and this is particularly appreciated in those applications where complex shapes of fillers are required. A preliminary distinction of metal foams' applications could be done considering just the porosity or the level of openness of the cells, between structural and functional applications. A higher relative density generally characterizes the first while the latter have a higher porosity, but there are some applications in between, as noticeable in Figure 1.16.

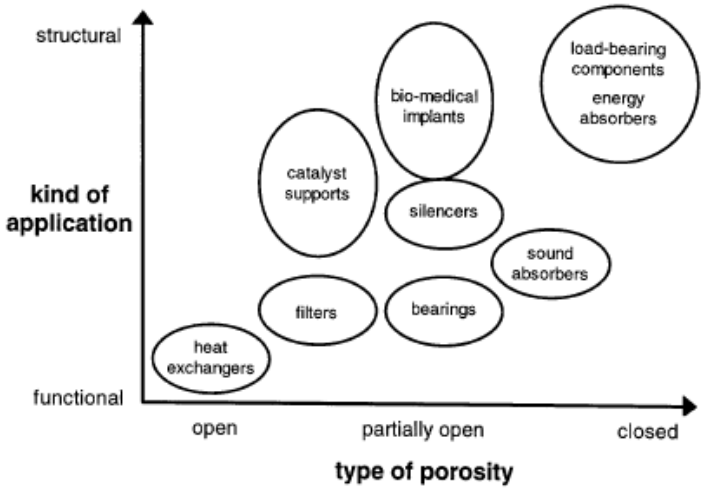

Figure 1.16: Application-porosity diagram for metal foams [5]

1.3.1 Light weight structures

Light weight construction depends on two properties of metallic foams: they exhibit a range of almost reversible, quasi-elastic deformation and their stiffness-to-mass ratio is high. As regard the latter property, just considering that a flat panel made by foams with, e.g., one fifth of the density of a bulk metal, have bending stiffness-to-mass ratios, which are five times higher than that of conventional sheets of the same weight (see the demonstration in Figure 1.17). Very often, a thin sheet of bulk material is added on the faces of metal foams structure, thus forming a sandwich panel. In these panels the stiffness-to-mass ratio is even better because the bulk material placed on the extremities will absorb the higher stresses, when loaded in bending. In reality, foam-based structures have to compete with conventional structures with optimized mass distributions: aluminum foams should be compared with aluminum extrusions, aluminum foam sandwiches with aluminum honeycombs or waffle-stiffened panels. Foam-based structures nevertheless can be preferable because:

- Easier to manufacture in a given complicated geometry;

- More robust and damage tolerant (the failure behavior would be less catastrophic);
- They exhibit additional properties such as noise reduction and heat resistance

Figure 1.17: Bjorksten demonstration of both lightness and stiffness of Al foam [1]

Metal foams and sandwich panels are used as structural components in automotive and aerospace industry. In particular, Boeing has evaluated the use of large titanium foam sandwich parts made by the gas entrapment technique and aluminum sandwiches with aluminum foam cores for tail booms of helicopters. Moreover, the possibility of making composite panels (Figure 1.18.b) with a metal foam core between metallic or composite sheets pushes large interest by the aerospace industry.

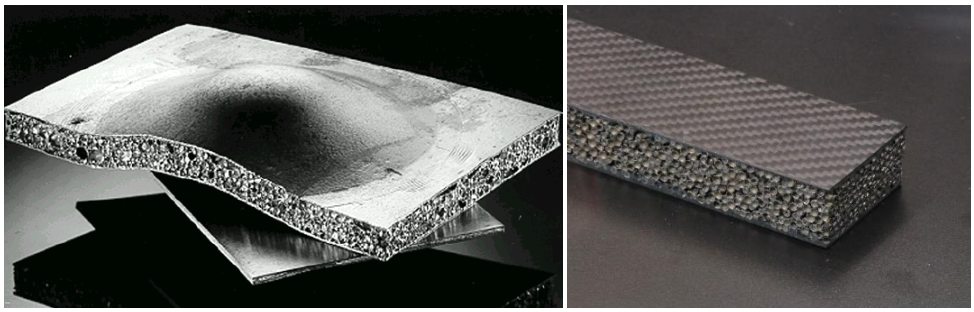

a) *b)*

Figure 1.18: a) aluminum sandwich panel; b) carbon fiber-aluminum hollow sphere foam sandwich panel [10]

1.3.2 Crash energy absorption

Many cellular solids are excellent energy absorbers owing to their deformation at a nearly constant stress level over a wide range of strain, but metal foams might outperform conventional foams because of their much higher strengths. This is the main reason why these materials have already found large use as energy absorbers, especially in automotive industry. In particular, what really makes metal foams exceptional is:

- their almost rectangular stress (σ_{pl})-strain behavior especially for foams with high porosity;
- a high absorption capacity per volume, length or mass unit;
- isotropy of energy absorption (except for some cases where the manufacturing route creates anisotropies)

Depending on the body to whom the absorber will be mounted, the thickness h of the foam can be designed as:

$$h = \frac{1}{2}\frac{mv^2}{\sigma_{pl}\varepsilon_D A} = \frac{1}{2}\frac{v^2}{a^*\varepsilon_D}$$

where m and v are the mass and the speed of the body, while σ_{pl} and ε_D are the plateau stress and the densification strain of the foam (see Figure 1.7.a) and a^* is the deceleration of the body. Figure 1.19 shows the dependence of the thickness h for a given foam from the velocity and deceleration of the body.

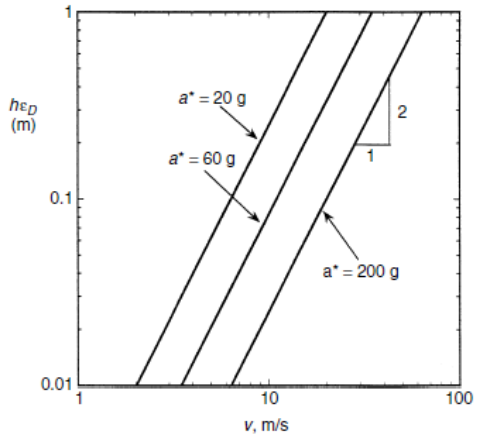

Figure 1.19: Thickness of the foam for different decelerations a [2]*

The effect can be even more pronounced if foam filled sections are compared with empty sections. A foam filling significantly changes the deformation behavior and failure mode of hollow sections and can therefore lead to additional absorption effects and weight savings. Examples of applications where foam-filled structures are crushed axially include crash boxes for head-on impacts or underride protectors for lorries, whereas crashing in the bending mode is involved in A- or B-pillar reinforcements or in other side impact protections [5] (see Figure 1.20 and Figure 1.21).

Figure 1.20: Aluminum foam components for crash absorption in automotive industry [11]

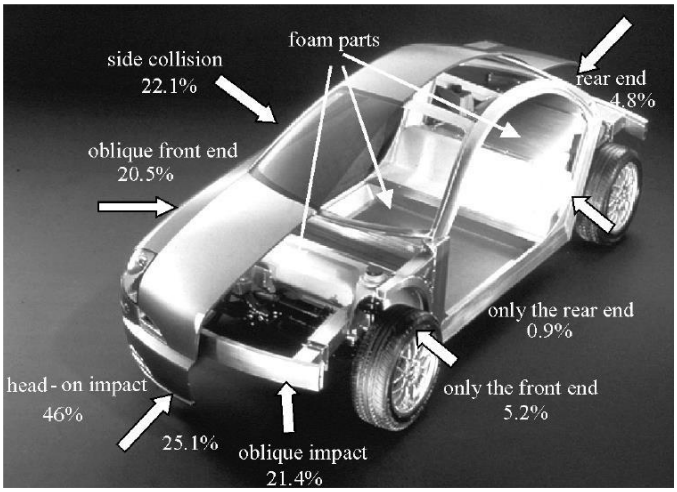

Figure 1.21: Karmann car with parts made of aluminum foam [12]

1.3.3 Biomedics

Titanium or cobalt–chromium alloys are used for prostheses or dental implants because of their biocompatibility. Figure 1.22 shows a hip joint made by titanium foam: bulk titanium has a higher elasticity modulus and weight than titanium foams, but the latters have values of density and young modulus close to natural humans' bones.

To ensure ingrowth of tissue, one usually produces a porous layer of the same or another biocompatible material on the prosthesis by thermal spraying or other methods. Moreover, magnesium foams could be used as bio-degradable implants which serve as load-bearing structure as long as the bone still grows but are gradually absorbed by the body in a later stage of convalescence.

Figure 1.22: Titanium made by preformed hollow spheres used for a hip prosthesis. [13]

1.3.4 Functional

Traditional powder metallurgy (PM) has created porous sintered metals for a wide scope of applications. Metal foams follow this tendency of porous materials, finding many functional applications mainly as silencers, filters and heat exchangers.

Silencers and vibration absorption

A sound wave that falls onto a porous material is partially reflected and partially enters the structure. A part of the entering wave is absorbed while the remaining wave is transmitted. The reflected wave is attenuated by destructive interference whenever the surface of the foam is not completely closed. The coefficient of absorption (α)of a sound wave is defined as:

$$\alpha = 1 - \left(\frac{B}{A}\right)$$

where A and B are the amplitudes of the pressure incident wave and the one reflected respectively. Figure 1.23 shows the level of sound absorption of Alporas foam in a range of 0.8-3 kHz. It is possible to notice that after 10% compression the absorption level is higher especially for higher frequencies.

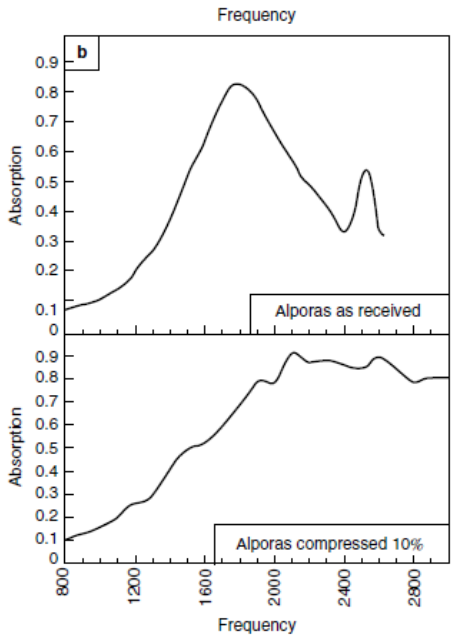

Figure 1.23: Sound absorption of virgin and compressed Alporas foam: Frequency [Hz] [2]

Panels of Alporas foam have been used as sound absorbers along motorways and other busy roads in Japan to reduce traffic noise (see Figure 1.24) and in the Shinkansen railway tunnel to attenuate sonic shock waves, or for indoor sound absorption purposes in entrance halls of public buildings.

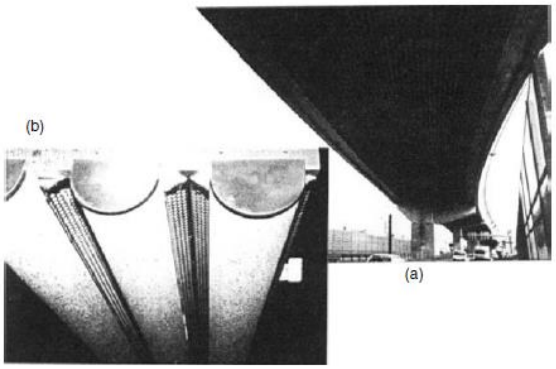

Figure 1.24: Sound-absorbing lining on the underside of a highway bridge [2]

Filters

Important filter properties are fine filtration capacity, good particle retention, cleanability, mechanical properties, corrosion resistance and cost. Metal foams characterized by an open structure and a high level of porosity can be used as effective and durable filters for both liquids and gases.

Figure 1.25: Example of filter made by metal foams [14]

Heat exchangers

Highly conductive open cell foams based on copper or aluminum can be used as heat exchangers or transpiration cooling. Heat can be removed from or added to gases or liquids by letting them flow through the foam and cooling or heating the foam at the same time. Metal foams can perform better if they are selected in a way that thermal conductivity is kept as high as possible with their flow resistance maintained as low as possible. These two requirements are contradictory, so a compromise has to be found. Examples of heat exchanger made by metal foams are like the one in Figure 1.26.

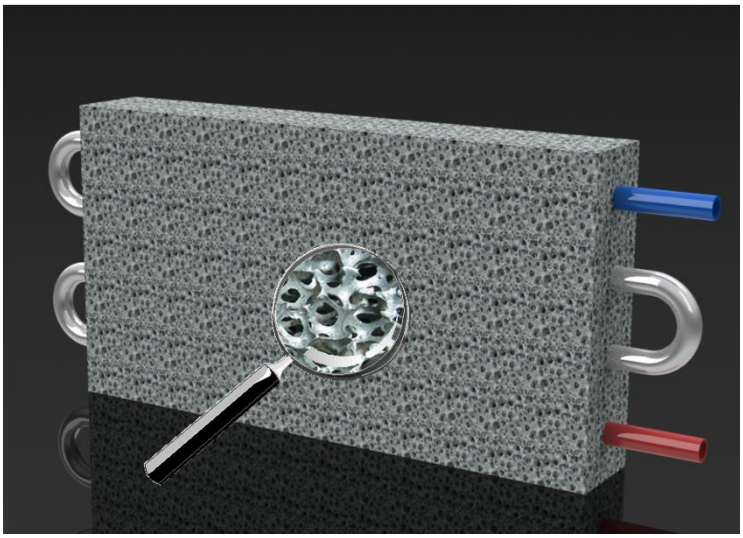

Figure 1.26: Heat exchanger developed by Freunhofer institute [15]

Chapter 2) Materials and specimens

2.1 Benefits of filling tubes with foam

When it comes to structural applications, metal foams are generally accompanied by bulk materials, giving birth to sandwiches, tubes and so on. Filling a tube or a panel with a metal foam leads to an obvious increase in weight but at the same time stiffness, damping capacity and energy absorption are largely improved. Therefore, choosing a foam-filled structure is a very good compromise between leaving it empty and making it bulk.

Impact absorption is the most studied characteristic of foam-filled tubes. Thin-walled metal tubes are efficient energy absorbers when crushed axially. By 'efficient' we mean that the energy absorbed per unit of volume or per unit weight is high. When a foam is compressed, its cell walls bend and buckle at almost constant stress until the cell faces impinge. The tube behaves in a different way: it buckles into a series of regular ring-like folds until, when the entire tube has buckled, the fold faces come into contact [2] (see Figure 2.1.a). Figure 2.1.b shows the load-deflection curves for the compression of a foam, a tube and a foam-filled tube. The energy absorbed corresponds to the area below the load curve. The tubes show regular wave-like oscillations of loads, each wave corresponding to the formation of a new fold, while foam shows a smoother and lower curve. The interesting and surprising result stand

in the fact that the foam-filled tube has a higher collapse load and a higher energy absorption than the sum of the curves of foam and empty tube.

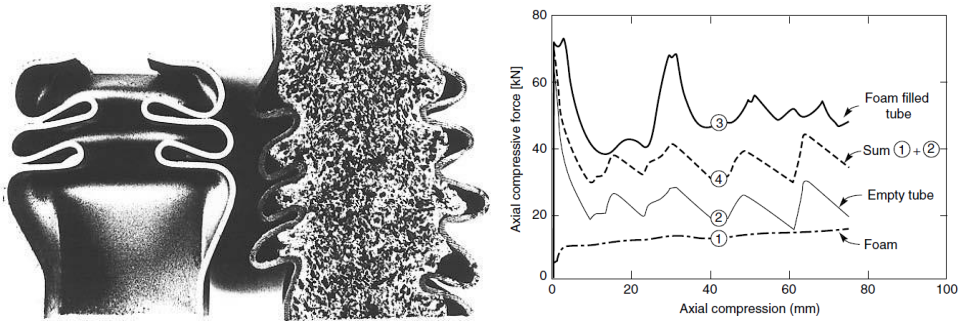

a) *b)*

Figure 2.1: a) Empty tube and foam filled tubes after partial crushing; b) Load curves during compression for foam, empty tube and foam-filled tube [2]

Even bending stiffness is highly improved by foam filling. In [16], Zarei and Kröger performed bending crash tests on empty and Alporas foam-filled square aluminum beams. Usually, the bending collapse of thin-walled beams is localized in a plastic hinge and the other parts of the beams undergo a rigid-body rotation. Due to small rotation angle, local collapse occurs in the beam and its resistance drops significantly, which results in low energy absorption efficiency. The insertion of the aluminum foam has a noticeable effect on increasing the bending resistance of the aluminum tubes.

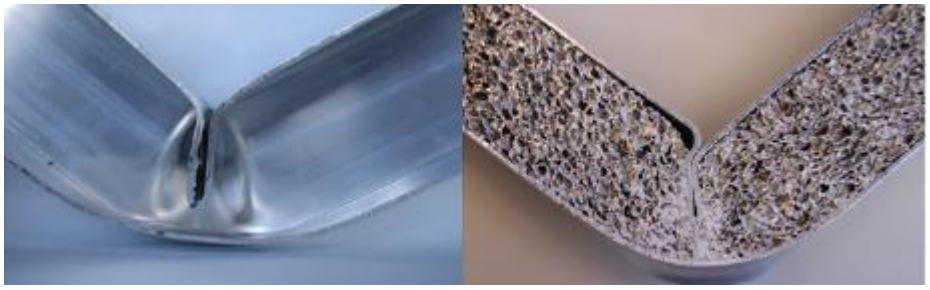

a) *b)*

Figure 2.2: Bending behavior of empty beams (a) and foam-filled beams (b) [16]

2.2 Foam-filled titanium tubes

We decided to make and test titanium tubes filled with aluminum foam because of the interest shown by *Bell Helicopter Textron Canada*. In fact, titanium is particularly used in aerospace industry thanks to its low density and exceptional resistance to corrosion. Moreover, the addition of aluminum foam brings all the advantages described previously at the expense of a modest increase in weight. Table 2.1 lists the main characteristics of this material.

Name	ρ	E	Tensile Yield Point	Melting Point
Titanium Grade 2	4510 Kg/m3	105000 MPa	275-410 MPa	1665 °C

Table 2.1: Some properties of titanium used for tubes [17]

We decided to create specimens that could be portions of real tubes possibly used in helicopter industry, but not only. In doing this, we chose to provide ourselves whit titanium tubes with an external diameter of 38 mm. The others geometrical details of the specimens are listed in Table 2.2.

Figure 2.3: Examples of foam-filled titanium tubes

Dimension (nominal)	[mm]
External diameter of tube	38
External diameter of foam	36
Thickness of tube	1
Length of the specimen	215

Table 2.2: Geometry details of the tubes

2.2.1 Preparing procedure

The preparation of these tubes follows the foaming process described in 1.1.2. First, we place Alulight precursors (whose characteristics are in Table 1.1) inside the titanium tube and we close its extremities with two stopper. Then, we place the tube inside a mold, as the one in Figure 1.4.b, and the mold inside an air convention furnace, preheated at 750°C, for about 13 minutes. Once out of the furnace we extracted the tube from the mold, and we cooled it with a compressed air flux. During cooling, the tube is rotating to let the foam solidify homogeneously and have almost the same local density in the tube. In Figure 2.4 the crucial steps of the foaming process. Since the melting point of titanium is at about 1665°C, the precursors start foaming at about 600°C and the maximum temperature reached in the furnace is 750°C, the tube does not melt and no intermetallic between titanium and foam is observed (see Appendix 2: , for details). Consequently, the titanium tube gives the shape to the foam, and remains its container after cooling.

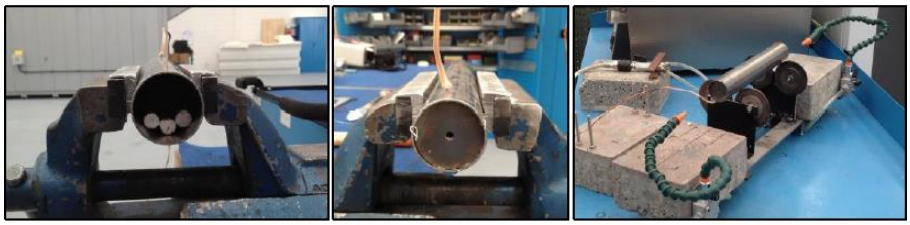

Figure 2.4: Sequence of foaming process: a) placing the precursors in the tube; b)closing the extremities with stoppers; c) air cooling after foaming while the tube is rotating [18]

Once the tube is cooled, the stoppers are removed and the extremities are cut obtaining the final length of 215 mm. This final cut is done both to remove the extremities that are inhomogeneous and to create an aluminum burr that somehow forces the foam inside the tube. In fact, since there is no intermetallic, if no burr is formed the foam would be able to move inside the tube (helped by shrinkage after cooling) only hampered by friction. Obviously, the metal burr cannot represent a stable and rigid bond so that some phenomenon of micro friction occur, especially far from the extremities. Some examples of the final product are in Figure 2.3.

2.2.2 Types of specimens

Not only one type of specimens is investigated in this work. We decided to make tubes filled with foams of different densities and having different interfaces between the foam and the tube. More precisely, for what concerns the factor *density* we made:

a) A foam with nominal density equal to 557 kg/m^3 (ρ/ρ_s = 0.21) obtained by using *3 precursors* for foaming.

b) A foam with nominal density equal to 815 kg/m^3 (ρ/ρ_s = 0.30) obtained by using *4 precursors* for foaming

The characteristics of Alulight AlMg1Si0.6 precursors were already given in Table 1.1. However, precursors' length changes between low and high-density foam as explained in Table 2.3.

Density of foam	# of precursors	Length of each precursors [mm]	Total nominal mass of precursors [g]
Low	3	210	143
High	4	227	206,2

Table 2.3: Number, length and mass of precursors for foaming low and high density

As for the density, two kind of *interface* are considered:

a) *Natural interface*: it is the spontaneous interface formed after the foaming process.

b) *Bonded interface*: the commercial Hysol® 9466™ epoxy glue bonds the external surface of the foam and the internal surface of the tube together.

See Appendix 1: "Foam-Tube Interfaces" for any details on the natural interface and bonding of tube and foam. Table 2.4 shows some detail of the tubes investigated in this work. We made 3 specimens for each combination of the levels of factors density and interface, for a total of 12 specimens.

Name/Code	Density of foam [Kg/m^3]	Type of Interface	Measured mass [g]	Estimated density of foam [Kg/m3]	Estimated relative density ρ/ρs
A40_10	Low	Free	278.58	557.9	0.212
A40_11	Low	Free	280.18	564.6	0.215
A40_14	High	Free	339.56	813.4	0.309
A40_16	Low	Glued	279.38	548.3	0.208
A40_17	Low	Glued	280.13	551.5	0.210
A40_18	Low	Glued	279.69	543.8	0.207
A40_19	Low	Free	277.19	553.2	0.210
A40_20	High	Free	339.80	815.4	0.310
A40_21	High	Free	338.33	809.3	0.308
A40_22	High	Glued	340.17	802.5	0.305
A40_23	High	Glued	340.06	799.0	0.304
A40_24	High	Glued	339.00	796.8	0.303

Table 2.4: Foam-filled titanium tubes details

2.3 Foam filled steel tubes

These tubes are different from the previous ones in both geometry and materials. The section is no more circular but square and the dimensions are bigger. At the extremities, there are two flanges inclined at 45° respect to the longitudinal axis of the tube. Each flange has 8 holes for bolted shortcuts. In fact, these flanges give the possibility to make bi-dimensional assemblies with tubes. Figure 2.5 and Table 2.5 detail their geometry.

Dimension (nominal)	[mm]
External geometry of tube	50x50 (square)
External geometry of foam	46x46 (square)
Thickness of tube	2
Length of the specimen	500

Table 2.5: Geometrical details of foam-filled steel tubes

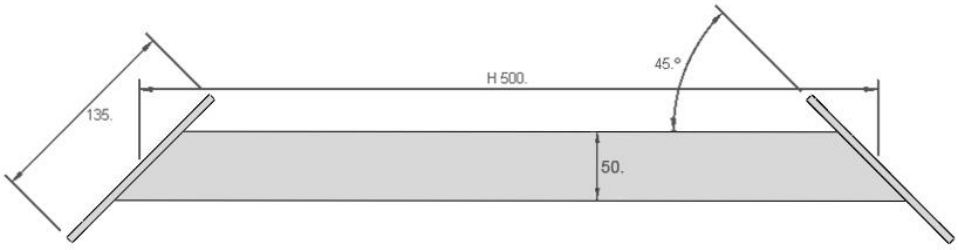

Figure 2.5: Dimensions of steel tubes

The material of the external tube is structural steel S235 whose main characteristics are in Table 2.6. The use of steel is justified for low budget applications and when light structures are not strictly necessary, not sacrificing stiffness at the same time. This is the reason why this tubes where

conceived for structural use in machine tools field, where the loads are high and dynamic and a good damping capacity is really appreciated.

Name	ρ	E	Tensile Yield Point
S235	7850 Kg/m^3	200000 MPa	235 MPa

Table 2.6: Some properties of steel uses for tubes

2.3.1 Preparing Procedure

Alulight precursors foaming

The aluminum foaming procedure is similar to the one executed for titanium cylindrical tubes. Alulight precursors are placed in the tube as in Figure 2.6.a. Two bolted steel endplates were fixed on the flanges in order to limit the foaming expansion outside the tube. Then the tube was placed horizontally inside a furnace preheated to 700°C for about 11.5 minutes and then cooled in a compressed air flux. The result is the foamed section visible in Figure 2.6.b.

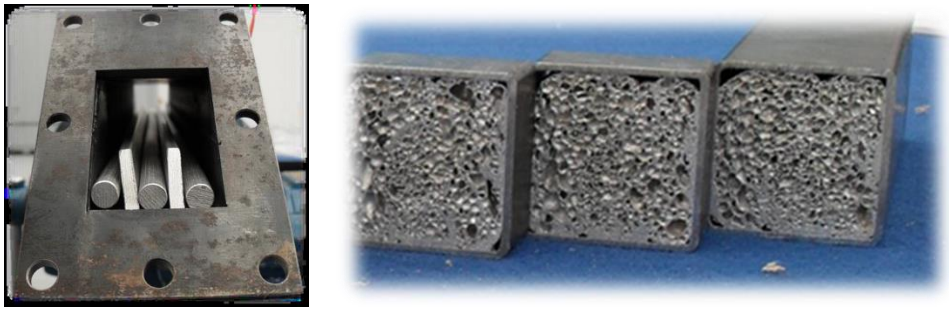

a) *b)*

Figure 2.6: a) Precursors in steel tube; b) foamed section

It is appropriate to specify that this foaming process consists of a heat treatment close to the normalization for the steel tube. The mechanical properties such as Young's modulus and yield strength are unchanged but the material shows a more ductile behavior during yielding, due to microstructure distention.

Hybrid APM foaming

The Advanced Pore Morphology (APM) process is a method for production of aluminum foam-polymer hybrid materials. Aluminum spheres produced by foaming a granulated precursor are then coated with a thermoplastic polymer adhesive that contains a chemical foaming agent. In our case, these coated spheres were put into the steel tubes with two endplates mounted to maintain the spheres inside. The tubes were then placed horizontally into a furnace, which was preheated to 160 °C and were kept at this temperature for three hours, to effect the foaming and curing of the adhesive. The filling of the tube with coated spheres and the result of foaming are in Figure 2.7.a and Figure 2.7.b respectively. Furthermore, the temperature reached during the foaming process is as low as to not affect any of the characteristics of the steel tube.

a) *b)*

Figure 2.7: a) APM spheres filling the tube; b) APM foamed section

2.3.2 Specimens

The specimens tested in this work are:

- 2 aluminum foam-filled tubes with nominal density of the foam equal to 550 Kg/m^3.
- 2 hybrid APM foam-filled tubes with nominal density of the foam equal to 490 Kg/m^3
- 2 empty tubes

The specified characteristics of each tube are in Table 2.7.

Name/Code	Type of Foam	Nominal density of foam [Kg/m^3]	Measured total mass [g]	Estimated density of foam [Kg/m3]
116	APM	490	2534	515.09
117	APM	490	2525	511.28
122	Alulight	550	2582.5	548.38
123	Alulight	550	2575.5	550.76
7	None	/	2017	/
9	None	/	2014	/

Table 2.7: Characteristics of steel tubes

Chapter 3) Modal analysis of foam-filled titanium tubes

The object of this chapter is to study the modal characteristics of the *cylindrical foam-filled titanium tubes*. This is done in order to investigate the *damping* capacity of these tubes and how it changes depending on the type of *interface* between tube and foam and on the foam's *density*.

3.1 Experimental setup

A description of the way we carried out the experiments follows:

a. We connected each specimen to a nylon cable, simply letting the cable pass through the holes on the base surface of the foam, and we suspended it in the air. The cables were all 1 m long approximately. We made this choice in order to make the external damping and the transversal force as low as possible during the vibration of the tube. Indeed, this is a good approximation of the ideal free-free boundary condition.

b. We attached a high sensitivity accelerometer (see 3.1.1) on the external surface of the tube, on the bottom side (as in Figure 3.1).

c. The hammering point was chosen on the top of the tube but on the same axial line of the accelerometer. This choice is to let the transversal vibration be almost all on the same plane of the accelerometer and minimize vibrations on the perpendicular plane. In any case, the accelerometer is mono-directional and the vibrations on the perpendicular plane are supposed to be ignored.

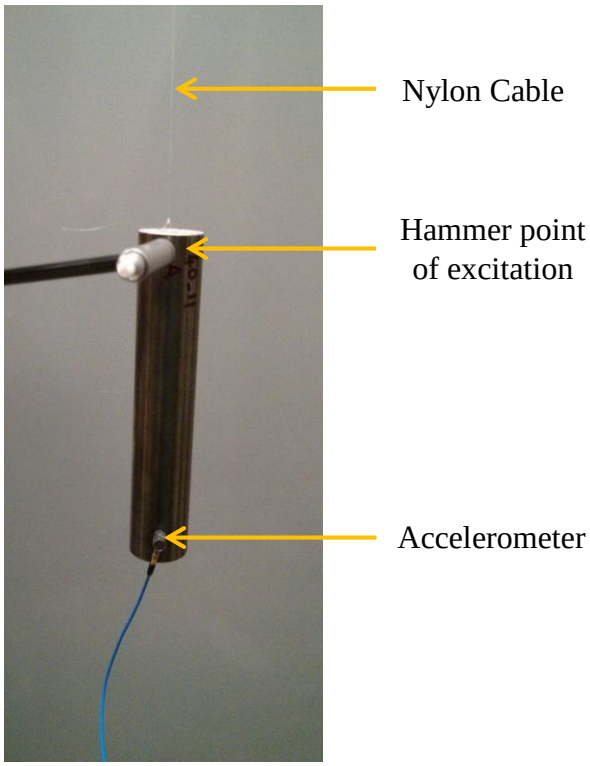

Figure 3.1: Impact test set-up

Each specimen (the list is in Table 2.4) was hammer-tested 5 times. Then the software made the time average of the five tests, in order to cut the noise, which was then considered as the final response to analyze.

3.1.1 Testing equipment

These series of test have been performed at *ÉTS* (*École de technologie Supérieure*) making use of the sensors and tools available there. Here is a list of the equipment used and its technical characteristics:

- PCB® Accelerometer, sensitivity of 100,8 mV/g and resonant frequency of 53,1 kHz;
- PCB® Impact Hammer, sensitivity 1,1 mV/N and resonant frequency > 22kHz;
- Acquisition System: LMS;
- LMS software for acquisition and analysis of the time history;

3.2 Results

3.2.1 Theoretical results and FEM Simulations

We made a finite element model, built on Abaqus® software, in order to have an idea of the natural frequencies (see Table 3.1) and the shape of the related traversal modes of vibration (Figure 3.2) of these tubes. The model considers 3D shell homogeneous elements for the tube and 3D solid homogeneous for the foam. Mechanical characteristics of foam, such as density and Young's modulus where known or estimated from previous tests. We chose a tie as a constraint between the tube and the foam: this condition simulates well the bonded interface but is quite far from the natural one. In fact, the aim of this simulation was to have only a predictable value of the natural frequencies and modes' shape, not to analyze deeply what happens on the interface between tube and foam.

Metal foams are particular materials because they can change their density having always the same shape and dimension. In this situation, increasing the density means an increase in mass and Young's modulus at the

same time. More precisely, for closed cells foam the modulus E scales with relative density as:

$$E = (0.1 \div 1.0)E_s\left(0.5\left(\frac{\rho}{\rho_s}\right)^2 + 0.3\left(\frac{\rho}{\rho_s}\right)\right) \qquad [2]$$

In our case the density was known for both the heavier and the lighter foam but E was known only for the lighter one and equal to 4000 MPa. Then, we estimated the Young's modulus for the heavier foam whit a proportional relation, such as:

$$E_h = E_l \frac{\left(0.5\left(\frac{\rho_l}{\rho_s}\right)^2 + 0.3\left(\frac{\rho_l}{\rho_s}\right)\right)}{\left(0.5\left(\frac{\rho_h}{\rho_s}\right)^2 + 0.3\left(\frac{\rho_h}{\rho_s}\right)\right)} = 6400\ MPa$$

where ρ_l and ρ_h are the lower and the higher densities while E_l and E_h are the Young's moduli of the lighter and the heavier foam respectively. Those values were used for the physical specifications of the finite element model.

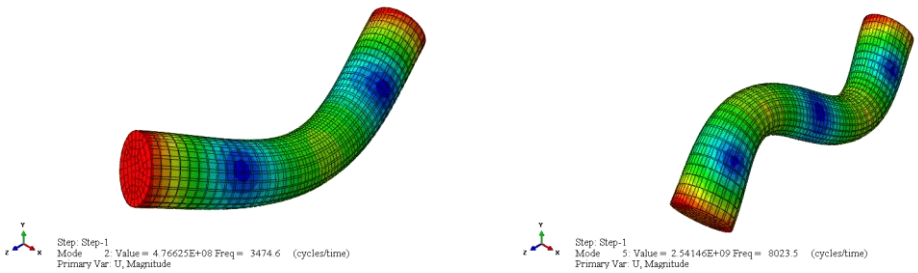

a) *b)*

Figure 3.2: a) first and b) second modes of vibration of cylindrical tubes filled with high density foam

Density of foam	1st Mode [Hz]	2nd Mode [Hz]
Low	3637	8305
High	3474	8023

Table 3.1: Simulation's natural frequencies for the first two transversal modes

It is possible to notice how the increase in density reflects in a light decrease in natural frequencies. Ashby in [2] proposes a scaling relation for the flexural and longitudinal natural frequencies of metal foams beams and tubes, as:

$$f_1 = \frac{C_1}{2\pi}\sqrt{\frac{EI}{m_0 l^4}}$$

where $m_0 = \rho A$, ρ is the density of the foam, A the section area and I the second moment of area. The moduli of foams scale as $(\rho/\rho_s)^2$, and the mass as (ρ/ρ_s). Thus the natural vibration frequencies of a sample of fixed dimensions scale as $f/f_s = (\rho/\rho_s)^{1/2}$, and so the lower the density of the foam, the lower its natural vibration frequencies. However, the result achieved with the FEM simulation and, as it will be shown later, with the experimental results is contradictory. It can be supposed that the effective Young's modulus of foams does not follow the scaling relation previously proposed. This can happens because of the unequal distribution of mass and so Young modulus in the piece due to inhomogeneity of the foam itself.

3.2.2 Experimental results

The amplitude response shown considers only in the 0:10000 Hz range, but the analysis develops until 20000 Hz (moreover, the 10000-20000 Hz spectrum range was characterized by low values of coherence in many data). Here some graphs follow showing an example of response for each type of specimen:

- *A40_17* and *A40_23* are respectively low density and high-density glued tubes. In this kind of specimen, the foam is not free to move inside the tube and, as it is possible to notice in Figure 3.3, the dynamic behavior is close to the ideal continuous body. In fact, natural frequencies and damping characteristics are easy recognizable. Moreover, it is possible to remark a difference in the value of the resonance frequencies between the high and the low-density tubes: the first show natural frequencies lightly smaller than the second ones.
- *A40_19* and *A40_21* are respectively low density and high density not glued tubes. Unlike the glued tube, this response (see Figure 3.4) is not so easy to analyze; many other frequencies, not visible through FEM simulation, seem to appear. This is probably due to the free movement of the foam inside the tube. The friction, between the foam's external surface and tube's internal one, brings to a noticeable increase in damping and introduces a lot of noise in the response. Thus, the coherence of these tests was generally sufficient (0.9) but unstable before 5000 Hz then decreasing constantly until reaching 0.5 after 8000 Hz. Again, a difference in natural frequencies between the lighter and the denser tube is noticeable. In this case it is hard to say whether the difference in weight of the tubes or the vibration of the foam inside play the most relevant role.

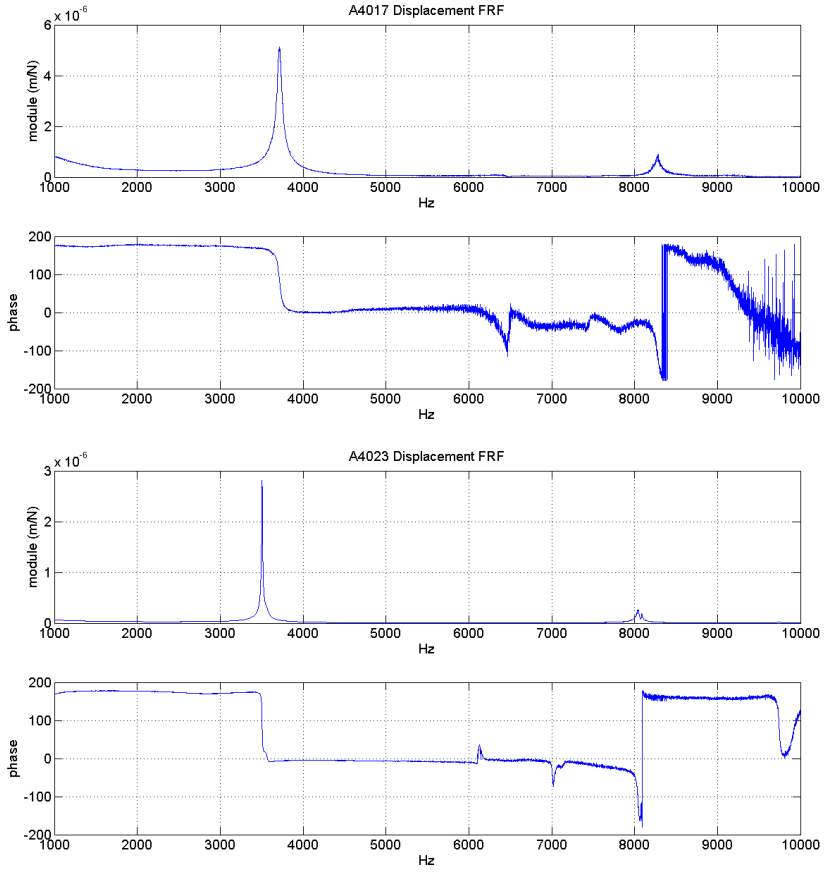

Figure 3.3: Example of FRF of glued interface specimens: A40_17 for low density and A40_23 for high density

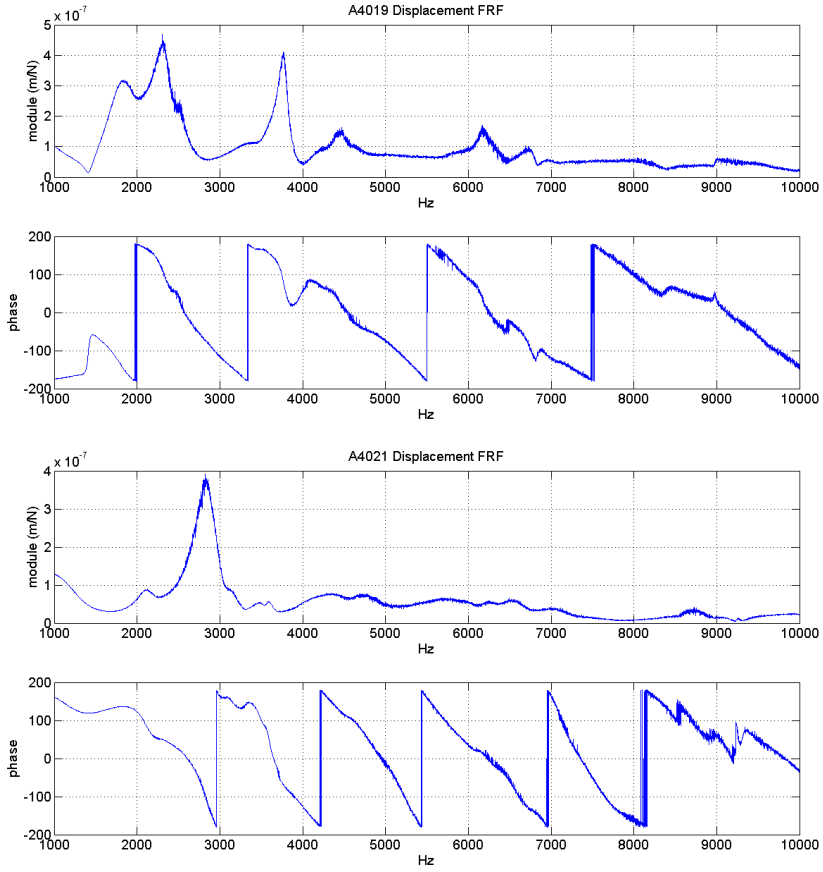

Figure 3.4: Example of FRF of natural interface specimens: A40_19 for low density and A40_21 for high density

For what concerns the damping characteristics of the tubes, we used the circle fit method to compute natural frequencies and damping ratio. Having a look to the response previously shown, it is easy to understand how the choice of the resonance peak was easy for the glued tubes but not for the natural interface ones. The presence of many other peaks introduces another random factor to the analysis. In order to be the most objective as possible in the choice, we decided to consider the most evident and isolated between the peaks close to the values given from the FEM simulation and so to the glued tubes natural frequencies. As a result, we computed two values of damping ratio for each specimen, one between 2500 and 4000 Hz and one between 6000 and 8500 Hz. These values are in Table 3.2. Giving a quick view to the data it is possible to notice how the interface condition seems to play the most

relevant role in determining the damping characteristics of the tubes: damping ratio is always above 1% for natural interface specimens while it is always below 1% for glued ones. The density, instead, does not seem to have any influence.

Name/Code	Density of foam [Kg/m^3]	Type of Interface	Low Resonance (2.5÷4 kHz)		High Resonance (6÷8.5 kHz)	
			Hz	ζ (%)	Hz	ζ (%)
A40_10	Low	Free	2747	3,3732	6857	1,6231
A40_11	Low	Free	3697	1,0388	7188	2,731
A40_14	High	Free	3685	1,4768	6752	2,4638
A40_16	Low	Glued	3725	0,5626	8267	0,2851
A40_17	Low	Glued	3717	0,722	8269	0,3407
A40_18	Low	Glued	3675	0,7899	8116	0,1509
A40_19	Low	Free	3762	1,4116	6130	1,5465
A40_20	High	Free	2982	3,5042	6726	1,6533
A40_21	High	Free	2820	2,8913	6549	2,0077
A40_22	High	Glued	3521	0,6897	7805	0,7518
A40_23	High	Glued	3505	0,164	8039	0,1902
A40_24	High	Glued	3526	0,6228	8040	0,288

Table 3.2: Values of natural frequencies and related damping ratios ζ for each specimen

With the help of Minitab® software, it is possible to perform a deeper and more rigorous analysis. We created a 2^2 factorial design where the main *factors* are:

1. *Density* of the foam: -1 for *low* density and +1 for *high* density
2. *Interface* condition: -1 for *natural* interface and +1 for *glued* interface

The number of replicates is 3 as the number of specimen for each combination of the levels of factors, for a total of 12 experiments. Then, we considered two *output*:

1. *ζ_low* as the damping ratio in the low resonance range
2. *ζ_high* as the damping ratio in the high resonance range

Figure 3.5 and Figure 3.6 show the Main Effects Plot and the Interaction Plot for the damping ratio in low frequency and high frequency ranges respectively. It easy to recognize the influence of the interface while the density and the interaction between the two factors do not seem to be significant in both cases.

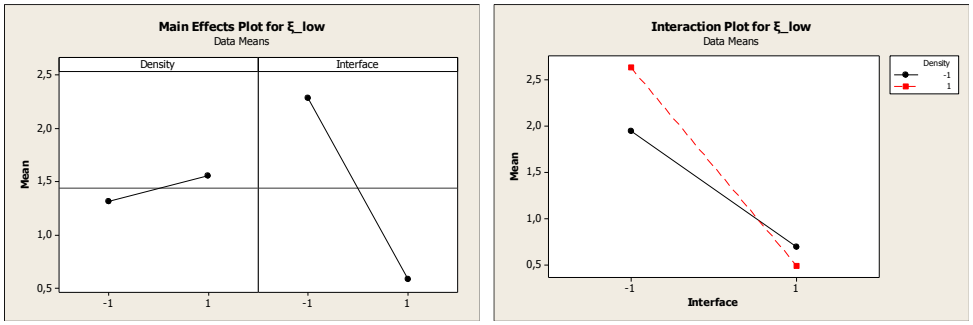

a) *b)*

Figure 3.5: a) Main effect and b) Interaction Plot for the low frequency damping ratio

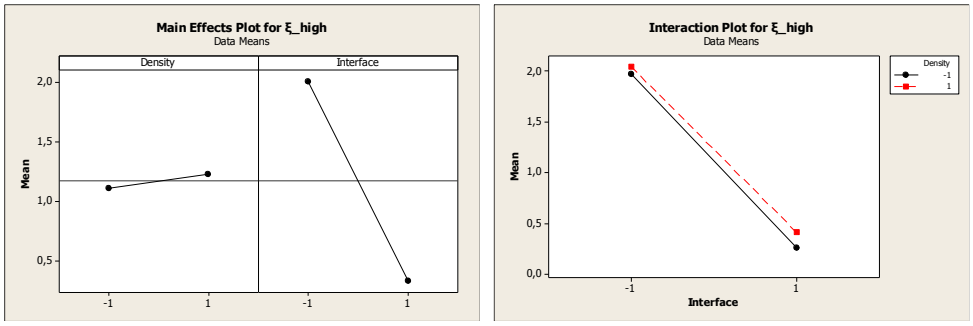

a) *b)*

Figure 3.6: a) Main effect and b) Interaction Plot for the high frequency damping ratio

After a preliminary analysis, the non-significance of the interaction was confirmed. Thus, we carried out a further analysis considering only the main factors in the model. The ANOVA table for both the cases is here reported:

Analysis of Variance for ζ_low (coded units)

Source	DF	Seq SS	Adj SS	Adj MS	F	P
Main Effects	2	8,7520	8,7520	4,3760	6,47	0,018
Density	1	0,1754	0,1754	0,1754	0,26	0,623
Interface	1	8,5766	8,5766	8,5766	12,69	0,006
Residual Error	9	6,0825	6,0825	0,6758		
Lack of Fit	1	0,5838	0,5838	0,5838	0,85	0,384
Pure Error	8	5,4987	5,4987	0,6873		
Total	11	14,8344				

Analysis of Variance for ζ_high (coded units)

Source	DF	Seq SS	Adj SS	Adj MS	F	P
Main Effects	2	8,40278	8,40278	4,20139	26,77	0,000

Density	1	0,03825	0,03825	0,03825	0,24 0,633
Interface	1	8,36453	8,36453	8,36453	53,30 0,000
Residual Error	9	1,41240	1,41240	0,15693	
Lack of Fit	1	0,00437	0,00437	0,00437	0,02 0,879
Pure Error	8	1,40803	1,40803	0,17600	
Total	11	9,81518			

They hypothesis of normality and homogeneity of variance of residuals between levels of each factor are satisfied for both the low and the high resonances damping ratio as it is shown in Figure 3.7 and Figure 3.8. This means that the model is valid and justifies the conclusions taken.

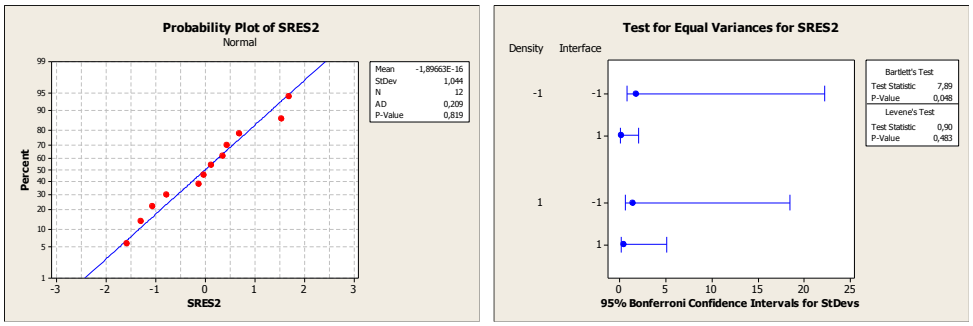

a) *b)*

Figure 3.7: a) Probability plot and b) Test for equal variances of residuals for the low frequency damping ratio

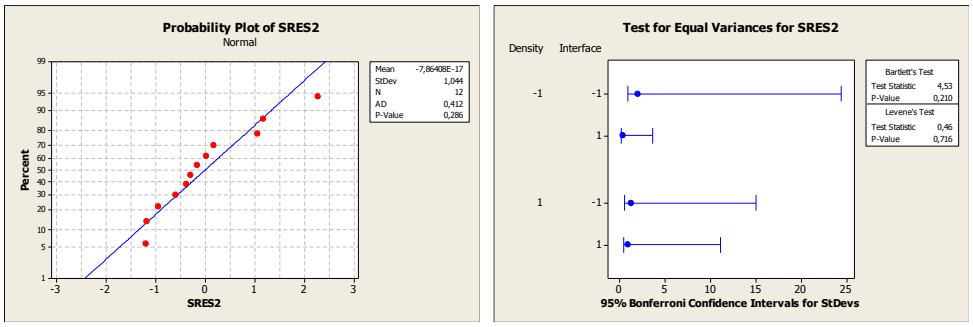

a) *b)*

Figure 3.8: a) Probability plot and b) Test for equal variances of residuals for the high frequency damping ratio

Moreover, it is possible to compute the power of the the factorial plan executed considering the estimate of the variance given by the MSE equal to 0.6873 and 0.176 for *ζ_low* and *ζ_high* respectively. The power value obtained are 0.958926 for *ζ_low* and almost 1 for *ζ_high* factorial plan. These values must be considered high for this kind of experimental test and then validating for the conclusions.

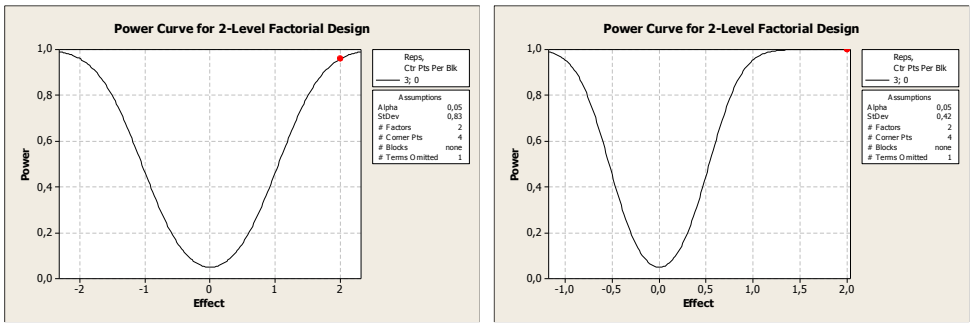

a) *b)*

Figure 3.9: Power curves for the factorial plan considering a) ζ_low and b) ζ_high MSE estimate for the variance

3.2.3 Discussion of results

From a qualitative point of view, the outstanding damping capacity of the natural interface was already noticeable from the FRF previously shown. Moreover, after the numerical analysis of experimental results, it is possible to conclude with a confidence level of 95% that the effect of the type of interface is influent on the damping ratio, while the density does not play any role in determining the damping capacity of these tubes and, indirectly of this aluminum foam. This can be obviously considered as a merit regarding those applications where damping is highly appreciated. On the other hand, high damping means high energy accumulated and so faster degradation and damage during the component's life. The next chapter will be investigating on the behavior of these tubes during cyclic dynamic loading, in order to state whether there is an influence of the interface and density on the mechanical performance of these potential components.

Chapter 4) Cyclic loading in bending

This chapter aims at investigating the behavior of aluminum foam-filled titanium tubes when loaded cyclically in bending. This is to simulate at least part of the loading life of these components once put in operation. Indeed, if used as structural parts of helicopters, vibrations induced by the rotor engine would constantly excite these tubes, as well as loads due to landing. The transversal displacement under constant amplitude of loading will be monitored in order to have the understanding of some changes inside the material. Furthermore, the acoustic emission signal will be acquired in order to understand the level of energy absorbed by internal damage or friction inside the tube, and to be compared to the displacement evolution.

4.1 Experimental procedure

4.1.1 Testing machine and fixtures

In performing the cyclic bending tests, we made use of MTS 810 testing machine (available at *ÉTS* laboratory), whose peculiarities are in Figure 4.1. This flexible and very accurate servo hydraulic machine can perform both monotonic and fatigue tests, and apply loads up to 100 kN. It can be

controlled in displacement or in force thanks to the information given by the load cell on the top cylinder. For any kind of control, a preliminary step of calibration is necessary before testing a new type of specimen. In our case, the control was in force.

In this study, a three point-bending test had to be performed, so that the usual grips for traction could not be used. In designing and manufacturing the fixtures for the bending test, we followed the Standard *ISO 7438 (Metallic materials- Bend test)*. This International Standard specifies the geometry of fixtures and the methods for determining the ability of metallic materials to undergo plastic deformation in bending.

The steel fixtures we used (see Figure 4.3) consist of a lower bar, two supports and a former. The lower bar is screwed into the lower cylinder of the machine, the two supports are screwed on the lower bar and the former is screwed into the upper cylinder. The standard says that the width of the supports and the former shall be greater than the width or diameter of the test piece. In our case, the diameter of the tube is 38 mm while the supports and the

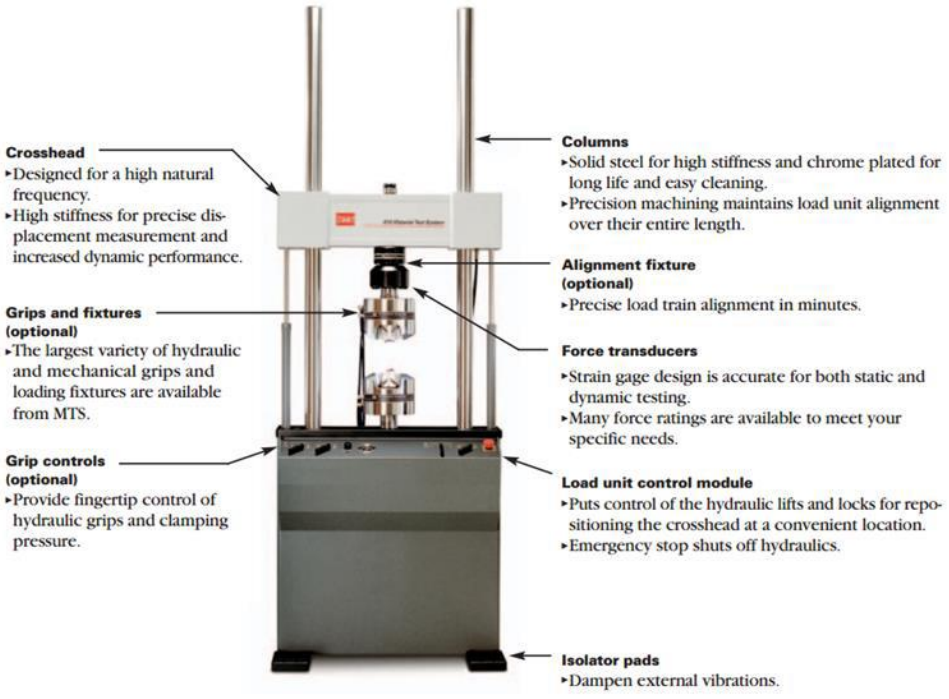

Figure 4.1: Details of MTS 810

former have the same geometry and width of 55 mm. Moreover, the standard gives a relation for determining the distance between the supports as:

$$l = (D + 3a) \pm \frac{a}{2}$$

where *l* is the minimum distance between the supports, *D* is the diameter of the former and *a* is the diameter of the test piece. Figure 4.2 details the geometry parameters. In our case the dimensions were:

$a = 38\ mm$

$D = 55\ mm$

$l = (55 + 3 * 38) \pm \frac{38}{2} = 169 \pm 19\ mm$

The lower bar of our fixtures has threaded holes placed on its upper surface for the supports screwing. The holes define three different position for the supports. In our case, the upper limit was the length of the specimens (215 mm) so we chose the available position whose distance between the supports was *210 mm*. Then the distance *l* was:

$l = 210\ mm - \frac{D}{2} - \frac{D}{2} = 155\ mm$

so inside the limits given by the standard *ISO 7438*.

The positions of the two supports was of course symmetrical so that the point of contact between the former was in the middle of the specimen.

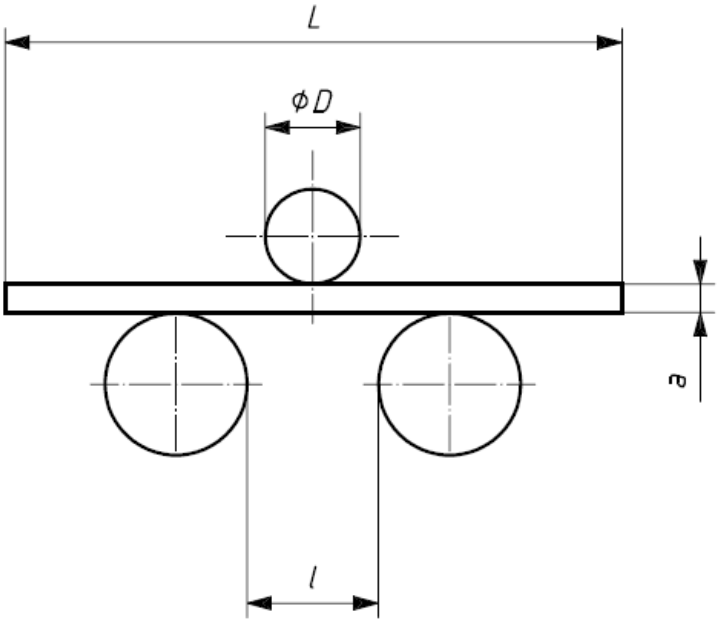

Figure 4.2: Geometry references for ISO 438

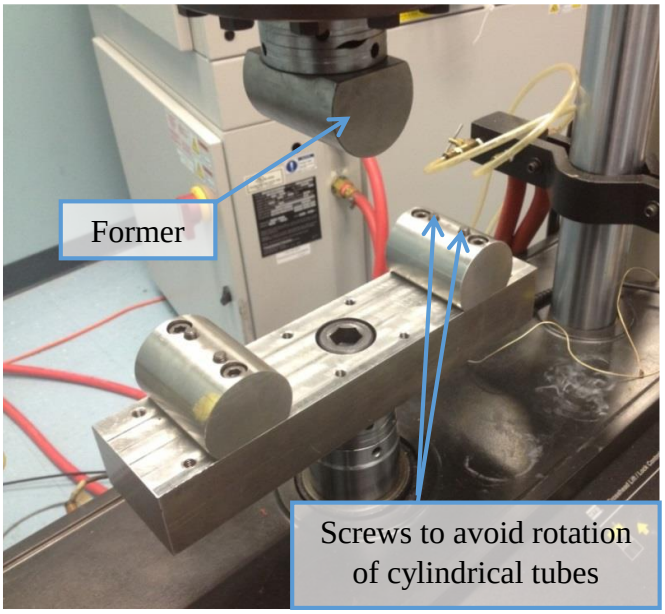

Figure 4.3: Fixtures' setup

4.1.2 Acoustic emissions' acquisition system

In performing cyclic three point bending tests, the acoustic signal coming from the specimen was recorded. In doing this, we believed in having an information about the microstructural failures and the overall energy absorbed during the cyclic loading.

We carried out acoustic emissions measurement using devices provided by Physical Acoustic Corporation (PAC). Two sensors (model Micro-80 PAC, bandwidth 100-1000 kHz) acquired the acoustic signal. Before each test, the quality of the coupling was verified through a Nielsen-Hsu pencil lead break. Through the mean of a tape, these sensors where fixed at approximately 35 mm away from the supports but on the upper side of the tube, in order to be not too close to the contact point of the supports, source of friction noise. A silicon adhesive gel was employed as a coupling agent between the surface of the sensor and the tube in order to improve the quality of the signal and avoid friction between the two surfaces. The signal of each sensor was then sent to an amplifier that gave 40 dB of gain to the voltage signal, and then to the PCI card, able to receive two signals in input. A representation of the measurement system is in Figure 4.4.

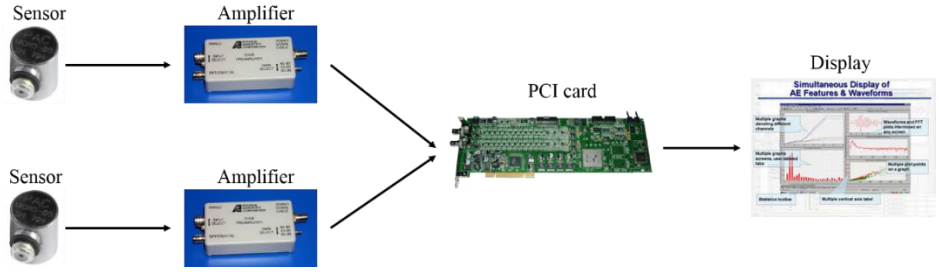

Figure 4.4: Schematization of acoustic emissions measuring system

The PCI card's sample rate was set to 2 MHz, in order to recognize frequencies in the sensors' bandwidth, while the acoustic threshold to filter background noise was set at 40 dB.

The quality of the measured AE data depends mainly on the choice of the waveform system timing parameters, namely, peak definition time (PDT), hit definition time (HDT) and hit lockout time (HLT). For detailed

information on these parameters and their importance, see Appendix 2: Acoustic Emissions. The values of the timing parameters employed are:

$$PDT = 300\ \mu s \quad ; \quad HDT = 600\ \mu s \quad ; \quad HLT = 1000\ \mu s$$

in accordance with the manual specifications for detecting cracks in metallic materials.

The software output is a series of events (or *hits*) related to a physical event that is happening during the test. For each event, the software computed parameters like *counts*, *duration*, *rise time*, *RMS*, *energy* of the signal and many others. These parameters are useful for analyzing what is really happening in the piece. Some research studies, such as [19] and [20], have been carried out to distinguish the different mechanism of failure through the analysis of acoustic emissions in metallic and composite materials. However, because of time and knowledge limits, here we limited our analysis at estimating the overall level of damage accumulated during fatigue.

Finally, the machine and instrumental setup is visible in Figure 4.5.

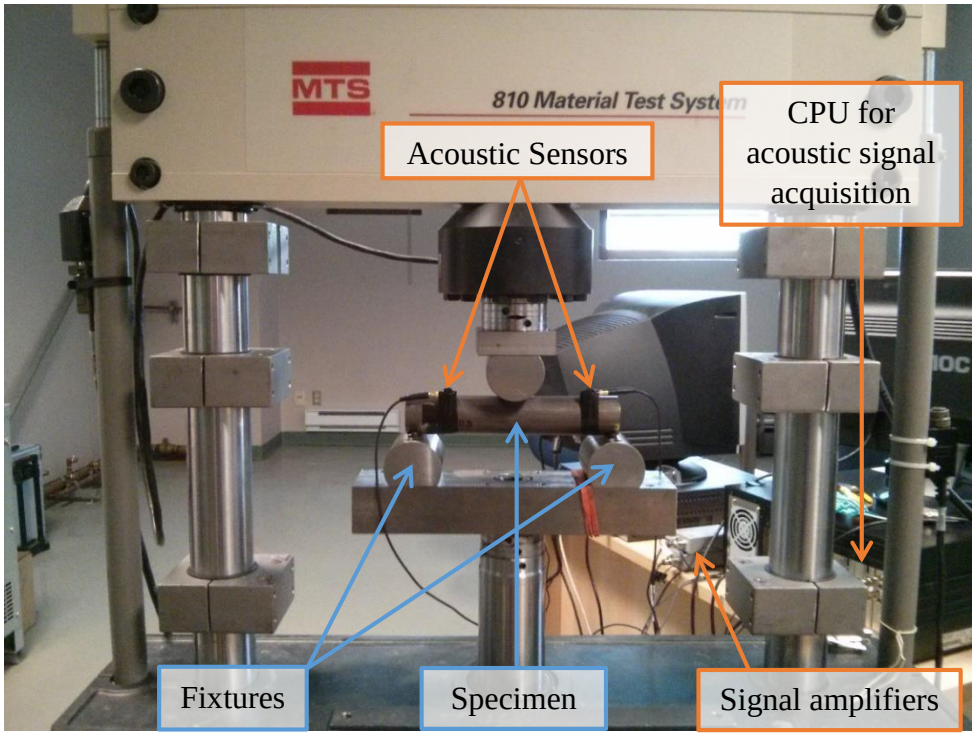

Figure 4.5: Test setup on MTS machine

4.2 Procedure

In defining the methods for the execution of these tests, two main parameters had to be chosen: the loading level (and so the stresses) and the number of cycles to perform. As a reminder, the purpose of this test was not to estimate the fatigue limit or the S-N curve of these materials. Indeed, preparing a standard specimen for traction fatigue test is something far from realizable for this kind of "composite" materials. Our intentions instead were oriented in analyzing the behavior of these potential structural components while loaded cyclically with a significant but non-destructive stress level.

In doing this choice, we referred to the previous bending tests done on these kind of tubes in [18]. In that work, Belfiglio firstly performed a cyclic step-loading test on low-density and high-density specimens with a natural interface, finding a quadratic trend in displacement for the first and a linear trend for the second. Subsequently he focused his attention on the lighter tubes, realizing that something irreversible due to plastic deformation was beginning when the maximum load was at 6 kN causing the non-linearity of the trend. Therefore, he performed tests of 10000 cycles with the maximum load step decreasing from 5 kN to lower values. Finally, he found that there was no significant difference in displacement, and so no plastic deformation between the beginning and the end of the test for a maximum load of 2 kN. Then he executed a 50000 cycles test with maximum load of 2 kN, but only for one specimen of low density foam and natural interface tube.

As already mentioned in 1.2.3, metal foams are more sensitive to the maximum level of stress than to the amplitude when cyclically loaded. Therefore, the critical choice was to find the maximum level of stress, and we decided to take into account the results achieved by Belfiglio. Moreover, proceeding in this way, a comparison between the specimens studied in this and that work is possible. Thus, the characteristics of the tests performed are in Table 4.1.

Parameter	Value
# of cycles	50000
frequency	10 Hz
Preload	0.5 kN
Maximum Load	5 kN
σ_{min}	0.0094 MPa
σ_{max}	0.038 MPa

Table 4.1: Characteristic of the cyclic bending test

A preload was necessary for bending tests, to avoid the detachment of the former from the test piece. The level of stress are far below the available endurance limits of metal foams (about some MPa), but this are inhomogeneous and unpredictable materials, thus damage can occur even at low stresses.

4.3 Results

Because of time issues, we could not test more than 4 specimens in total, so we decided to test a specimen for each combination of the factors *density* and *interface* condition. Therefore, the specimens tested are *A40_10* (low density-free interface), *A40_14* (high density-free interface), *A40_16* (low density-bonded), *A40_24* (high density-bonded), whose details are in Table 2.4.

The first interesting output is the displacement trend during the fatigue test. The MTS machine is able to give the maximum and minimum values of

displacement and force for each cycle. In the very firsts cycles the force had fluctuation of maximum 10% respect to the target values because of the adjustment of the piece on the fixtures, but after 500 cycles this transitory condition completely disappeared and the values where all in line with the setup ones. With regard to the displacement, these tests have confirmed how statistical and unpredictable the behavior of metal foams is. The displacement the machines gives in output refers to the relative displacement between the former and the fixtures.

Figure 4.6 and Figure 4.7 shows the maximum displacement (d_{max}) and the difference between d_{max} and d_{min} respectively for the low density (*A40_10*) and the high density (*A40_14*) free interface specimens. Regarding the *A40_10*, the maximum displacement has an almost linear trend for the first 1000 cycles, than it stabilizes quickly reaching almost a regime state at 5000 cycles. The difference instead does not seem to stabilize quickly, but smoothly decreases its derivative. Looking at *A40_14,* an opposite trend is noticeable: the maximum displacement does not stabilize while the difference reaches a constant value very quickly (almost in 1000 cycles), than has a soft linear growth from 8000 to 27000 cycles, and then remains constant for the rest of the test.

A sensible difference in the values of d_{max} and d_{max}-d_{min} is easy recognizable between the first and the second tube. This is clearly due to the difference in stiffness between the lighter (*A40_10*) and the denser (*A40_14*) foam. On the contrary, the instable behavior of the denser foam is not explicable through rigorous considerations, but it is possible to guess that a big defect, such as a largely bigger cell or particularly thin walls, due to the random structure of foams played an important role. The sudden increase of the difference d_{max}-d_{min} at about 8000 cycles, confirms that an irreversible and growing phenomenon, as a large crack, has happened to the material.

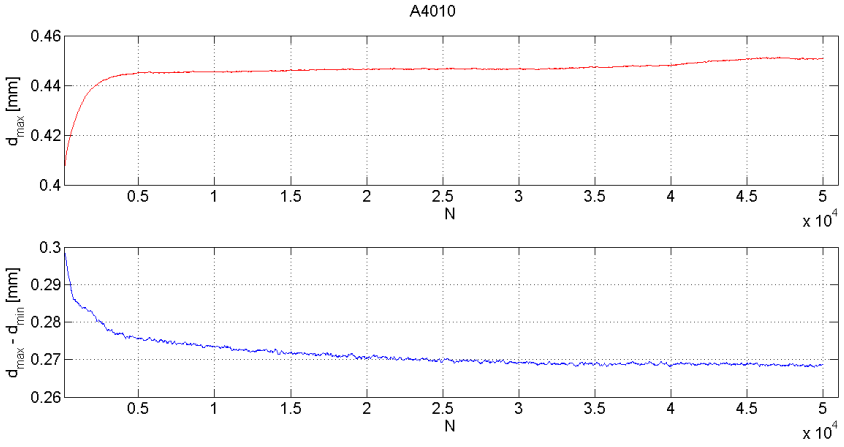

Figure 4.6: A40_10 displacements vs cycles (N)

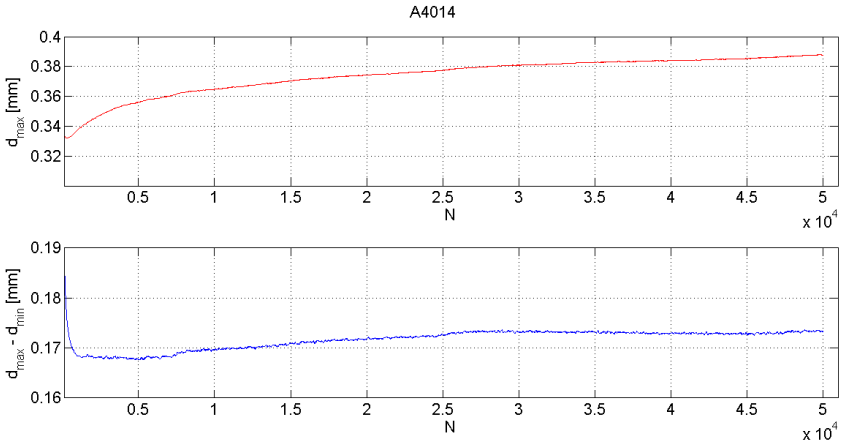

Figure 4.7: A40_14 displacements vs cycles (N)

Figure 4.8 and Figure 4.9 shows the behavior of the lighter (*A40_16*) and the heavier (*A40_24*) bonded interface tubes. These tubes have regular and equal behavior in both maximum displacement and difference of displacement: d_{max} has a logarithmic-like trend until 12500 cycles, then it increases linearly with an almost null derivative (especially for *A40_24*); the difference d_{max}-d_{min} quickly stabilizes as soon as the transitory in force stops, and is almost constant for the rest of the test. As for the non-bonded tubes, the values of displacements and difference are higher for the lighter foam and lower for the stiffer high density foam-filled tube.

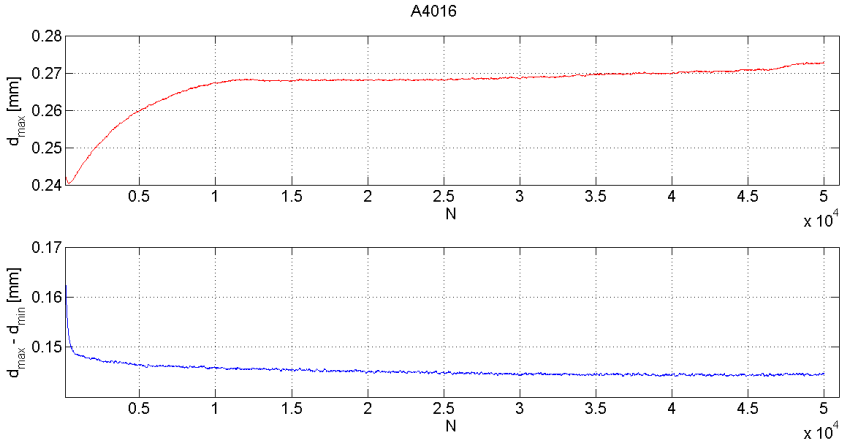

Figure 4.8: A40_16 displacements vs cycles (N)

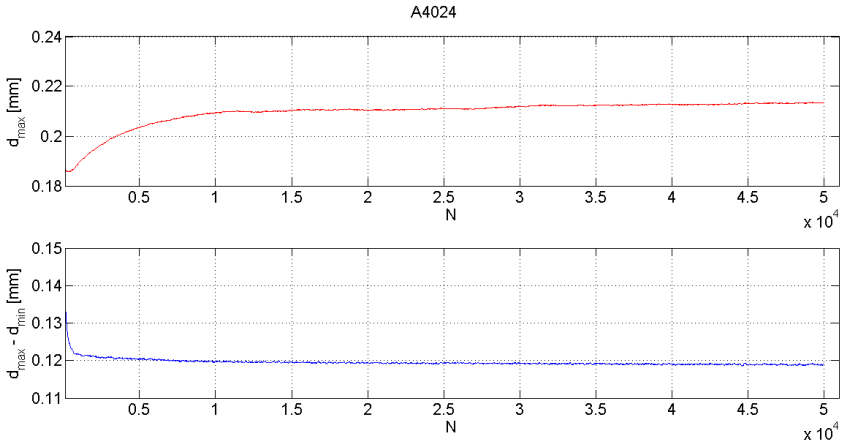

Figure 4.9: A40_24 displacements vs cycles (N)

Finally, it is possible to do some general considerations taking into account the information coming from these graphs. Table 4.2 summarizes the values of displacement for each test. The displacement d_{max} and the difference d_{max}-d_{min} are lower not only switching from low to high density, but even from natural interface to bonded one. This means that bonding the foam to the tube gives bending stiffness and better resistance to cyclic loading considering the behavior of the displacement difference. This is easily explicable considering that the natural interface gives to the foam the possibility to slide inside the tube, helped by the micro gap between the surfaces. On the contrary, the bonded interface forces the foam to follow the

same deformation of the external tube, giving more stability and stiffness to the tube itself.

Specimen	d_{max} (first cycle)	d_{max} (last cycle)	$\Delta(d_{max})$	d_{max}-d_{min} (first cycle)	d_{max}-d_{min} (last cycle)
A40_10	0.4065	0.4507	0.0442	0.2987	0.2886
A40_14	0.3321	0.3877	0.0556	0.1884	0.1733
A40_16	0.2404	0.2728	0.0324	0.1664	0.1447
A40_24	0.1856	0.2134	0.0278	0.1362	0.1191

Table 4.2: Summing up the evolution of displacement of each specimen tested. Values are in [mm]

4.3.1 Mechanical work absorbed during fatigue

Thanks to having the values of force and displacement for each cycle of the test, it is possible to estimate the energy absorbed by the specimen for deformation.

The mechanical work is a form of energy defined as:

$$W = \int_{x_1}^{x_2} F \times dx = \int_{t_1}^{t_2} F(t) \times \frac{dx(t)}{dt} dt$$

where W is the mechanical work, F is the force transmitted to the body, x the displacement of the point of application of the force, and t is the time. In the cyclic loading tests performed in this study both the force and the displacement have a sinusoidal pattern that can be defined as:

$$F(t) = \left(\frac{F_{max} - F_{min}}{2}\right) \sin(\omega t) + \left(\frac{F_{max} + F_{min}}{2}\right)$$

$$x(t) = \left(\frac{d_{max} - d_{min}}{2}\right) \sin(\omega t) + \left(\frac{d_{max} + d_{min}}{2}\right)$$

where F_{max} and F_{min} are the maximum and minimum force, and d_{max} and d_{mix} the maximum and minimum displacement. In order to be synthetic we will call:

$$A = \left(\frac{F_{max} - F_{min}}{2}\right) \quad ; \quad B = \left(\frac{F_{max} + F_{min}}{2}\right)$$

$$C = \left(\frac{d_{max} - d_{min}}{2}\right) \quad ; \quad D = \left(\frac{d_{max} + d_{min}}{2}\right)$$

So the derivative of the displacement respect to time and consequently the mechanical work become:

$$\frac{dx(t)}{dt} = C\omega \cos(\omega t)$$

$$dW = F(t) \times \frac{dx(t)}{dt} dt =$$

$$= (A\, sin(\omega t) + B) \times C\omega\, cos(\omega t) = (AC\omega\, sin(\omega t)\, cos(\omega t) + BC\omega\, cos(\omega t))dt$$

then the finite mechanical work, integrating the previous equation:

$$W = AC\omega \int_{t_1}^{t_2} \sin(\omega t) \cos(\omega t) dt + BC\omega \int_{t_1}^{t_2} \cos(\omega t) dt =$$

$$= \frac{AC}{2} [\sin^2(\omega t)]_{t_1}^{t_2} - BC[\sin(\omega t)]_{t_1}^{t_2}$$

If the integration is done on the whole cycle, this equation correctly gives a null value as output. However, our intention is to divide the entire cycle in a loading part and unloading one, taking advantage of the information of displacement and force for each peak of each cycle. Figure 4.10 explains this situation: for both the force and the displacement, a sinusoidal pattern is given for the loading (red) and unloading (blue) part of the cyles, considering a time lag of π/ω. More precisely, the loading cycle considers MIN(i) and MAX(i) to compute the amplitude, while the unloading cycle will consider MAX(i) and MIN(i+1).

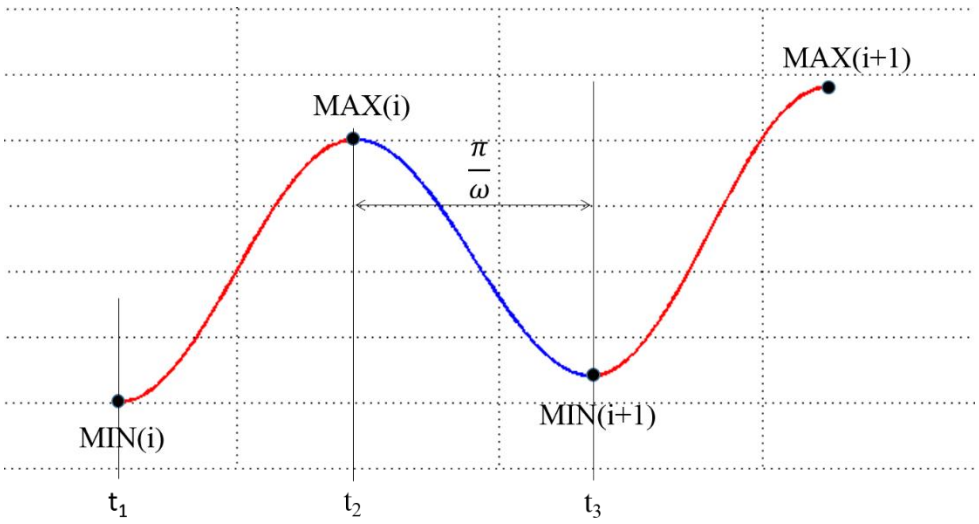

Figure 4.10: Cycles of loading (red) and unloading (blue) for the force and the absolute value of the displacement

Thus, for each complete cycle, going from MIN(i) to MIN(i+1), the energy for the loading part (W_1) and the unloading part (W_2) will be computed as:

$$W_1 = \frac{A_1 C_1}{2}[\sin^2(\omega t)]_{t_1}^{t_2} - B_1 C_1 [\sin(\omega t)]_{t_1}^{t_2}$$

$$W_2 = \frac{A_2 C_2}{2}[\sin^2(\omega t)]_{t_2}^{t_3} - B_2 C_2 [\sin(\omega t)]_{t_2}^{t_3}$$

Considering that the integration extremes are:

$$t_1 = -\frac{1}{2}\frac{\pi}{\omega} \quad ; \quad t_2 = \frac{1}{2}\frac{\pi}{\omega} \quad ; \quad t_3 = \frac{3}{2}\frac{\pi}{\omega}$$

it will be that:

$$[\sin^2(\omega t)]_{t_1}^{t_2} = [\sin^2(\omega t)]_{t_2}^{t_3} = 0$$

$$[\sin(\omega t)]_{t_1}^{t_2} = -2 \quad \text{and} \quad [\sin(\omega t)]_{t_2}^{t_3} = 2$$

Thus, the energy for the loading and unloading cycles will be:

$$W_1 = 2B_1 C_1 = 2\left(\frac{F_{\max(i)} + F_{\min(i)}}{2}\right)\left(\frac{d_{\max(i)} - d_{\min(i)}}{2}\right) = F_{med1} \times \Delta d_1$$

$$W_2 = -2B_2C_2 = -2\left(\frac{F_{\max(i)} + F_{\min(i+1)}}{2}\right)\left(\frac{d_{\max(i)} - d_{\min(i+1)}}{2}\right)$$
$$= -F_{med2} \times \Delta d_2$$

Finally, the total energy absorbed for the generic i^{th} cycle will be the difference between the absolute values of the loading work and the unloading work:

$$W_{absorbed(i)} = W_{1(i)} + W_{2(i)} = |W_{1(i)}| - |W_{2(i)}|$$

$$W_{tot} = \sum_{i=1}^{N} W_{absorbed(i)}$$

where W_{tot} is the total energy absorbed by the tube in the whole test.

Figure 4.11 shows the behavior of the energy absorbed during the test by each specimen. As it was expected, the tubes with a bonded interface absorb less energy than the ones with a natural interface. Moreover, the tubes show higher values for lower density and vice versa. The trend is very similar to the one observed for the displacement d_{max}: indeed the mechanical energy absorbed by the material is due to plastic deformation or development of cracks or in general the level of structural damage accumulated inside the piece.

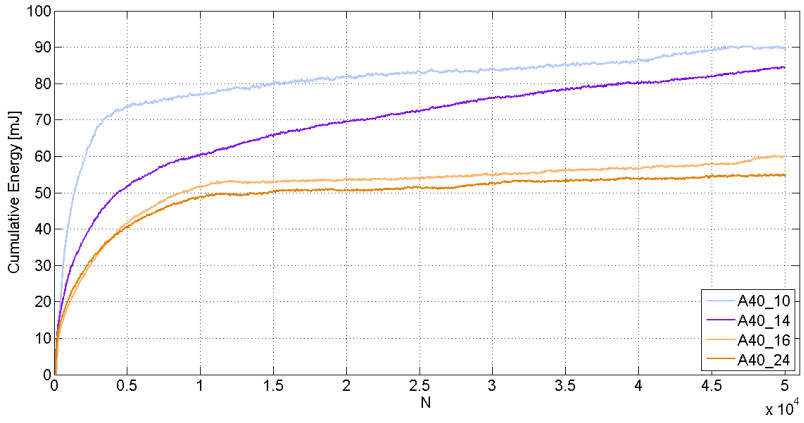

Figure 4.11: Mechanical work or energy absorbed during the test for each specimen

4.3.2 Acoustic emission signal

For each test, a series of events (hits) was recorded. More precisely, when the acoustic signal overcomes the threshold of 40 dB the software records the event, but only if it does respect the limits given by PDT, HDT, HLT (see Appendix 2: "Acoustic Emissions" for more details). For each event, many parameters concerning the acoustic wave are calculated. However, we focused our attention on the cumulative counts and cumulative energy (of the signal) of all the series of events during the test.

While the mechanical work mostly gives an idea of the plastic deformation accumulated in the piece tested, the acoustic emission (AE) analysis gives more information about any kind of internal damage occurring (plastic deformation, crack nucleation and propagation, large fractures and crack jumps, friction). For each specimen tested, we computed the cumulative energy of the signal [mV*s], and the cumulative counts evolution during cyclic loading.

Figure 4.12 and Figure 4.13 show the graphs respectively for the low density and high density natural interface-tubes. The trend is linear with some fluctuations for both the specimens. Nevertheless, there is a difference of one order of magnitude between the two specimen in both the energy and the counts. This difference can be linked to the different behavior of maximum displacement that the two tubes showed in Figure 4.6 and Figure 4.7. In that moment, we supposed that a large defect could have been responsible of the continuous growth of d_{max} during the test of *A40_14*. Now, the same large defect can be responsible of the stronger AE activity as well, causing this large difference.

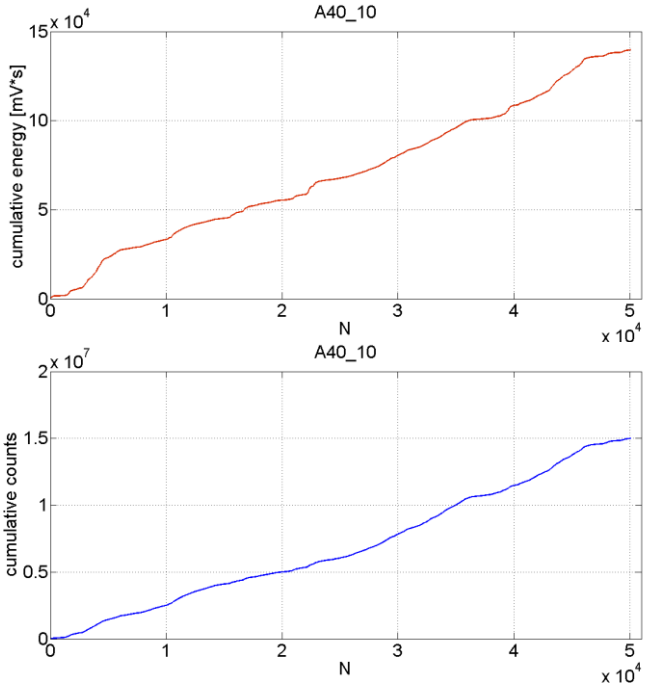

Figure 4.12: AE graphs for A40_10

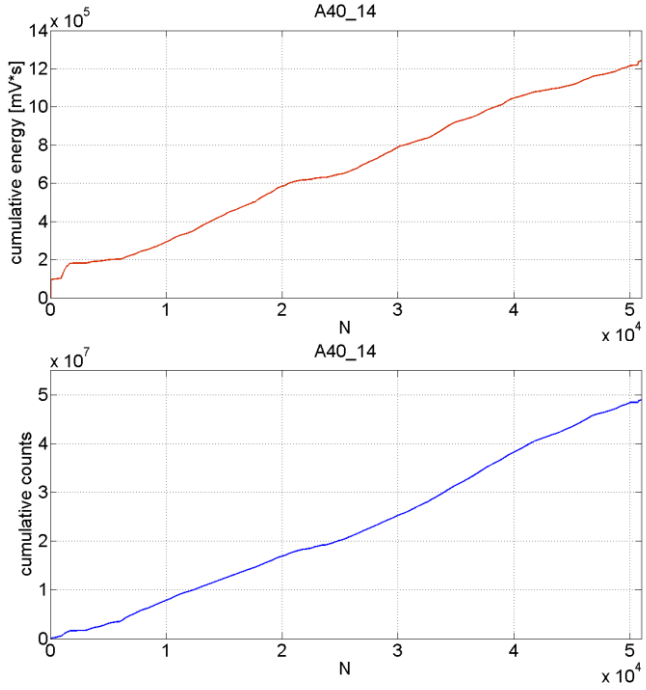

Figure 4.13: AE graphs for A40_14

Figure 4.14 and Figure 4.15 show the energy and counts evolution of the lighter and denser bonded interface-tubes. The trend is no more linear but piecewise linear. According to literature [20], when a piece of material undergoes fatigue, the AE activity steeply increases in the very first cycles because of adjustment, than has a slow (almost constant) linear trend during the movement of dislocation and cracks crowing, and then exponentially increases when large crack propagates, or the whole section collapse. However, this behavior is typical of bulk materials and there are no studies that describe clearly how metal foams behave. Indeed, none of the specimens tested truly follows that behavior, but *A40_16* and *A40_24* show a similar trend in some moments of the test. *A40_16* grows logarithmically during the first 12500 cycles (as its displacement d_{max}), then linearly and then almost exponentially after 35000 cycles. *A40_24* instead has a very rapid growth in the first 500 cycles (for adjustment), then slowly increases until 17000 cycles when it starts a faster linear growth to the end of the test. The order of magnitude and the values reached both in energy of the signal and counts are very comparable between the two different tubes and to AE levels shown in other studies: this means that no particularly large defect were present or were propagating inside the specimens.

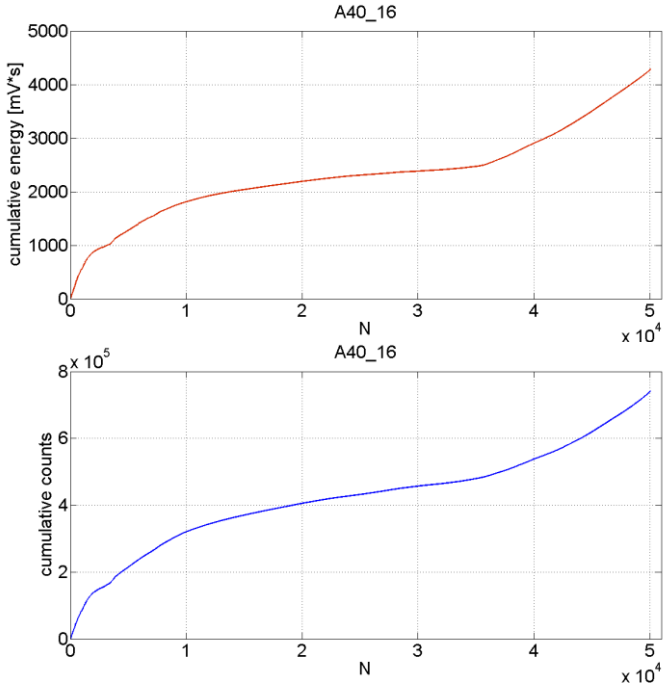

Figure 4.14: AE graphs for A40_16

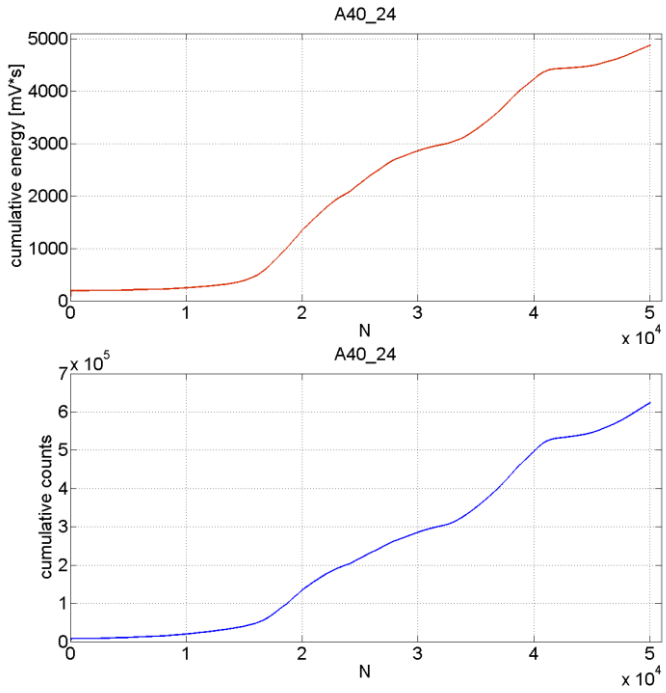

Figure 4.15: AE graphs for A40_24

Finally, the large difference between the non-bonded *interface* and the bonded one surely stands in the friction between the foam and the tube present in the first one. Friction is a source of sound emission at any frequencies and amplitudes, and in cyclic loading appears constantly for all the duration of the test. Evidently, it has a higher contribute to AE that the one coming from cracks and plastic deformation, so that somehow hides it completely when the overall energy or counts are plotted. It is a very difficult source of AE to cut because difficult to identify correctly, but at the same time it can be correlated to the level of microscopic damage accumulated in the material. Indeed, the mechanism of friction is a continuous succession of micro welding between the peaks of the irregular surfaces put in contact and its breaking. Thus, it can be truly associated to a form of degradation of the material that can cause the initiation of cracks. By the way, this confirms again how the natural interface is responsible of the higher energy absorbing ability of the tubes that are not bonded.

Chapter 5) 30 Hz damping test

The aim of this chapter is to estimate the contribution to low frequencies damping given by foam filling. This topic was pushed by the interest shown by Bell Textron Canada in making use of foam-filled tubes as structural components in helicopter field. These aviation machines have the unique ability to hover, take off and land vertically, and are so enabled to carry out many distinctive tasks in both civilian and military operations. Despite this, helicopter trips are usually unpleasant for passengers and crew because of high vibration level in the cabin. In addition to this, vibrations are also responsible for degradation in structural integrity as well as reduction in component fatigue life and for decreasing the effectiveness of onboard avionics or computer systems. Many techniques have been developed during the years to reduce the vibrations directly from the rotor through vibration control. Our intent, instead, is to add structural damping to the cabin and generally to the whole structure by the use of metal foams.

5.1 Test Design

The frequency and intensity of the vibration induced by the helicopter's rotor to the whole structure can vary depending on the dimensions and the

weight of the helicopter. As a rule of thumb, the lighter is the helicopter the higher is the frequency and the lower are the loads induced. However, Bell Textron Canada gave us a maximum reference value of 30 Hz.

In this work, we have already been speaking about damping characteristics for foam-filled titanium tubes. Nevertheless, in that case the damping ratio was computed for natural frequencies of some kHz. The dependence of aluminum foams from the frequency of vibration is generally supposed to be null [7], but we suspected that for so low values of frequency some changes in the expected results could occur.

The main difficulty we found was finding the way to make the foam vibrate at 30 Hz. The first option was to use a shaker vibrating at that frequency with a reasonable level of load. However, for such small bodies like the tubes studied in this work, attaching a shaker with its own non-negligible mass could introduce non-linearity and external damping, prejudicing the results. In spite of that, we switched our intent in building a tube or a structure vibrating in resonance at that frequency, in order to perform an impact test again. The first idea was to build a foam-filled titanium tube as long as to vibrate at 30 Hz in the free-free boundary condition (see 3.1), but the length of the tube would have been so large that a correct foaming process was impossible with the machines available in our laboratory. The last option, and then the final solution, came when we considered testing the foam-filled steel tubes (see 2.3). This kind of tubes have already been studied in our laboratory [18], in particular, a quadrilateral structure with two joint represented by two steel pegs screwed in a block of concrete (see Figure 5.1). One peculiarity of these tubes is the possibility of connecting them through the holes in the flanges building bi-dimensional assemblies. Thus, the idea was to build a cantilever assembly able to vibrate at about 30 Hz or less in resonance.

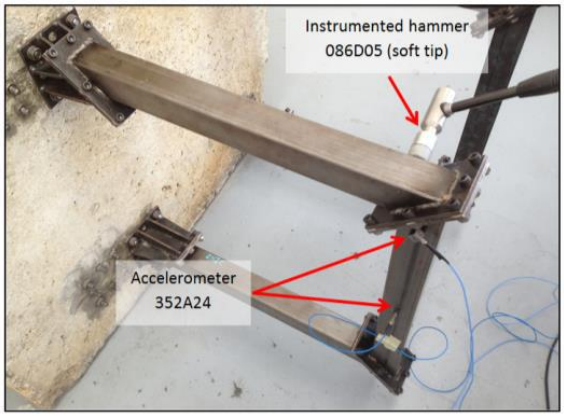

Figure 5.1: Structure studied in [18]

5.1.1 FEM simulations

A FEM model in Abaqus® was built in order to predict the resonance frequency. We made a model for the empty tubes structure and one for the aluminum foam-filled structure. The parts modeled are the peg for the joint, the steel tube, the aluminum foam and the washers put in between the bolding connections. The thin steel tube's wall were made by 3D S4R shell elements while peg, flanges, foam and washers were made by 3D C3D8 brick element. The average size of the elements is less than 5mm. The constraints are complete joint on the peg's surface facing the concrete block, tie between the faces of the washers and the two flanges (to simulate bolds' action on these surfaces) and tie between the external surface of the foam and the internal one of the tube for the foam-filled model. A preliminary simulation, considering a cantilever assembly with only one tube connected to the peg, showed a first natural frequency of 73 Hz. So we incremented the number of tubes to two, as shown in Figure 5.2.b, and the result for the foam-filled model was 22.8 Hz, sufficient for our intents. Then we executed a simulation for both the empty and filled models. The results are in Table 5.1 and the modes of vibration in Figure 5.3.

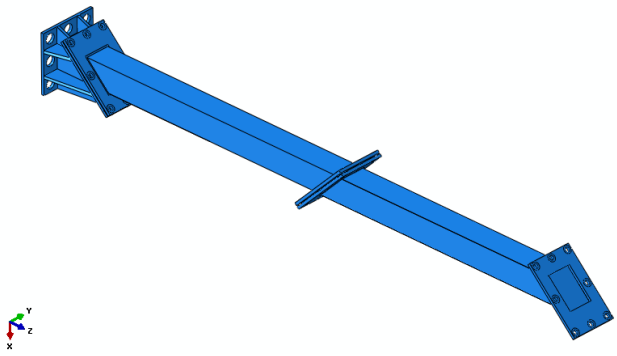

Figure 5.2: Model built for this study

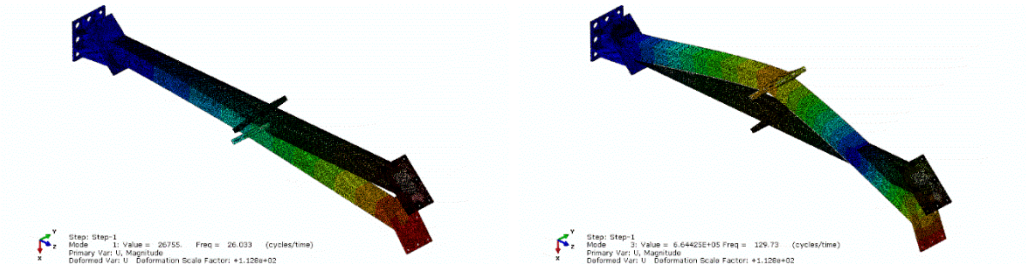

a) *b)*

Figure 5.3: a) First and b) second modes of vibration for the empty structure

Model	1st Mode [Hz]	2nd Mode [Hz]
Empty	26.0	130.0
Al Foam-Filled	22.8	116.3

Table 5.1: Natural frequencies for the empty and the aluminum foam filled structure

The values for the first mode are very satisfactory for both the structures, so the following step was to build and test the real assembly.

5.2 Experimental Test

5.2.1 Procedure and Set up

Each couple of specimen was connected one to the other and then one of them to the peg. Each connection consists of eight M8 steel bolts torqued at 25 Nm and 8 aluminum washers between the flanges. The measurement's system is characterized by 6 accelerometers placed on the structure as shown in Figure 5.4. The positioning choice was made in order to make the vibration modes shown in Figure 5.3 visible. The accelerometers are progressively lighter going from the peg to the free extremity: the weight is decreasing in order to avoid external damping on points with larger oscillations. The impact point was on the head of the extremity flange as shown in Figure 5.4, exciting mostly the modes previously described.

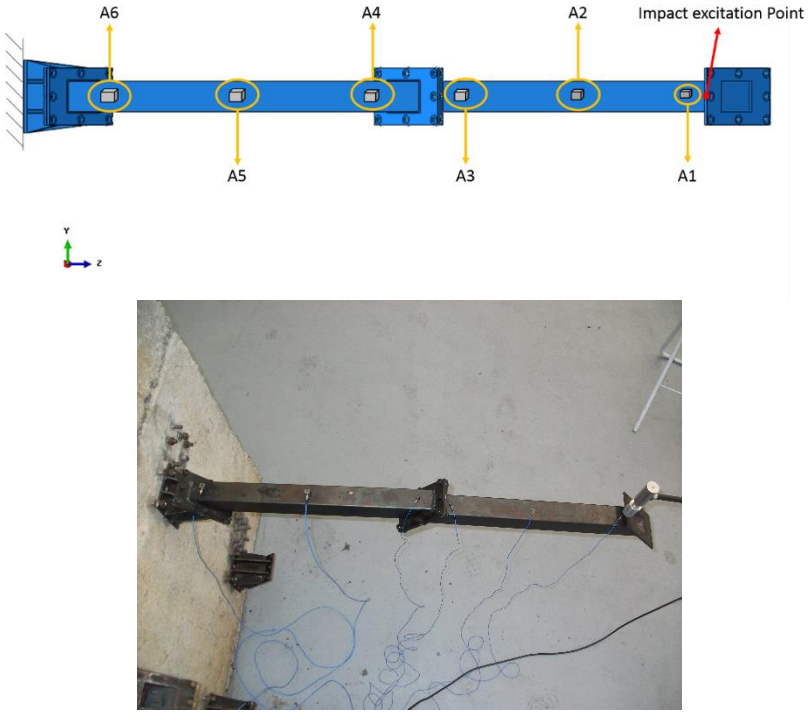

Figure 5.4: Position of accelerometers on the structure

Each structure was hammer tested 10 times. Then the software made a time averaging between the tests in order to filter the most of the noise. Furthermore, the hammer signal was windowed by a rectangular window of width 0.1s to cut frequency noise.

5.2.2 Testing Equipment

Table 5.2 shows the characteristics and the position of each accelerometer on the structure. The 0 reference for the z axis is considered on the peg's surface of contact with the concrete block.

Name (Code)	**Position along z axis [mm]**	**Sensitivity**	**Mass [g]**
A1 (PCB 352C23)	995	0.5 mV*s^2/m	0.2
A2 (PCB 352C23)	800	0.5 mV*s^2/m	0.2
A3 (PCB 352A24)	625	10.2 mV*s^2/m	0.8
A4 (PCB 352A24)	550	10.2 mV*s^2/m	0.8
A5 (PCB 356B21)	320	1.02 mV*s^2/m	4
A6 (PCB 356A32)	88	10.2 mV*s^2/m	5.4
Hammer (PCB 086D05)	995 (on flange)	0.23 mV/N	320

Table 5.2: Position and properties of the accelerometers

5.2.3 Results

The FRF of the A4 accelerometer for each structure is in Figure 5.5 for the empty structure, Figure 5.6 for the aluminum foam-filled one and in Figure 5.7 for the APM foam-filled one. We chose to show the response of

the A4 accelerometer because its position makes both the first and the second mode easily visible. Indeed, it is easy to recognize natural frequencies for all the three structures. The response of all the accelerometers of each cantilever structure tested was then analyzed in order to compute the modal parameters. Each response in the same structure was showing the same value of natural frequencies and damping ratios, which are listed in Table 5.3. Of course, this was not valid for the modal mass that was different for each accelerometer since the amplitudes were not equal.

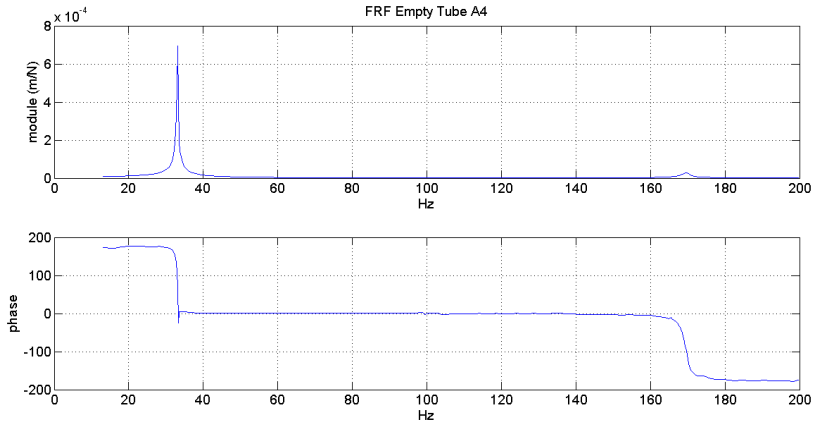

Figure 5.5: A4 FRF for the empty structure

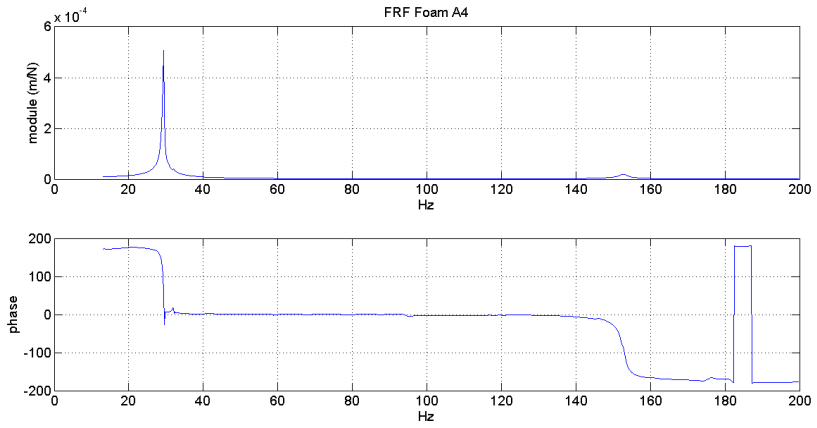

Figure 5.6: A4 FRF for the aluminum foam-filled structure

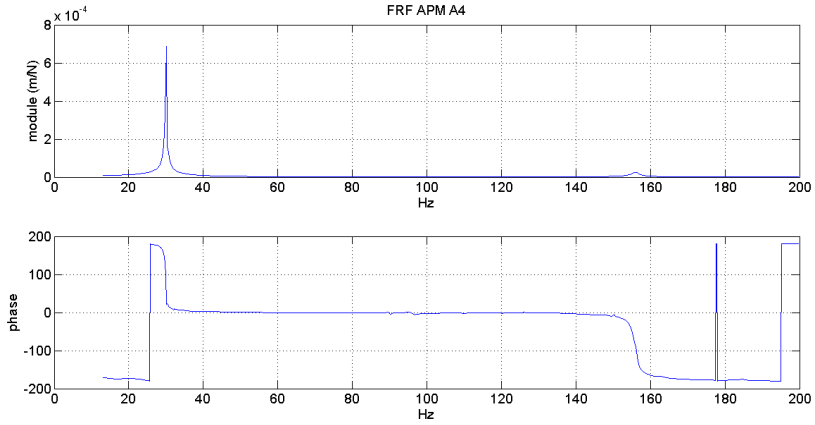

Figure 5.7: A4 FRF for the hybrid APM foam-filled structure

Mode of vibration	Empty		Alulight foam-filled		Hybrid APM foam-filled	
	Hz	ζ (%)	Hz	ζ (%)	Hz	ζ (%)
1st	33.2	5.6348	29.4	6.9851	30	5.3864
2nd	169.6	5.6221	152.8	7.9982	156	5.9192

Table 5.3: Natural frequencies and damping ratios for all the structures studied

The percentage of increment in damping ratio due to foam filling is shown in Figure 5.8. The Alulight foam improves significantly the damping characteristics, especially for the second mode of vibration .It is interesting to notice how the APM foam has a negative effect on damping for the first mode of vibration and a lightly positive effect on the second one. This is not a very surprising result considering that in [18] it was found that the APM foam had a lightly negative effect on bending modes of vibration.

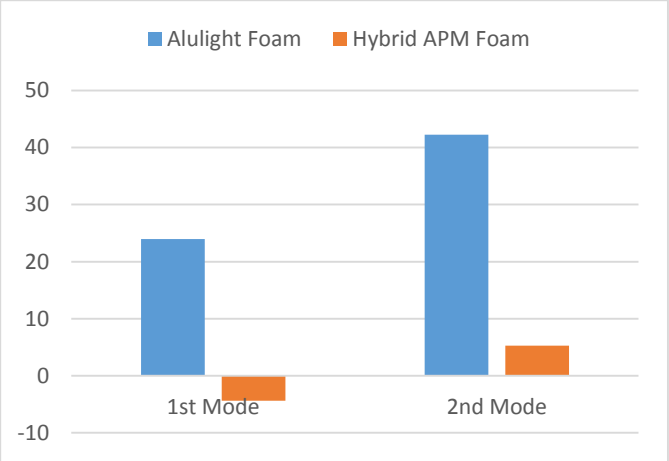

Figure 5.8: Percentage of increment in damping in 1st and 2nd mode for both the Alulight and APM foam-filling

5.2.4 Discussion of results

Generally, the damping characteristics of a structure are strictly related to the level of deformation, so that the higher is the amplitude of vibration, the higher are the deformation and the damping. The cantilever structure considered here has a particularly high deformation right close to the flanges' connection, as it is visible by FEM simulations in Figure 5.3. This already introduces a significant level of damping in the empty structure.

The hybrid APM foam is made by aluminum foam spheres kept together by an adhesive activated during foaming. This adhesive attaches to the internal surface of the steel tube, so that the foam is practically bonded. In Chapter 3) we have already explained how the natural (or free) interface has a better damping capacity than the bonded one. Thus, it can be supposed that the APM foam gives more structural stiffness to the tubes, lightly decreasing its deformation, and at the same time does not give a contribute to damping due to interface friction especially for the first mode at 30 Hz. On the other hand, the aluminum foam has the ability to increase the damping characteristics because both of the partial friction at the interface with the tube, both of the internal friction due to bending.

Chapter 6) Conclusions and further developments

This work partially confirms what previously thought about the advantages of foam filling. In Chapter 5) it is exposed how the damping capacity improved due to filling steel tubes with aluminum foam even when the frequency of vibration is as low as 30 Hz. In Chapter 3) it is pointed out how the natural interface improves significantly the damping ability of cylindrical foam filled titanium tubes. Furthermore, in Chapter 4) it is found out that the bonded tubes are stiffer and probably life longer.

In the light of what we discovered from this study, it is possible to recommend this components for structural purposes in aerospace industry and specifically helicopters. In assigning the specific use of this tubes, the designer should consider that denser tubes are of course heavier but stiffer (modulus of elasticity proportional to density). Moreover, whether high damping is required, natural interface specimens would give the best results, but at the same time they would accumulate more energy and probably have a shorter life. Indeed, corrosion, crack nucleation and crack growth (especially for aluminum, less corrosion resistant) are powered by the constant friction in vibrations.

Finally, many other investigations could be done on these interesting "composite" materials: other levels of density of the foam or other types of

interfaces (turned, sandblasted, etc.) or even other metals for the external tube. Although metal foam have been commercially available for at least 30 years, these materials are still not completely characterized. This is partially due to the inhomogeneity of its structure and partially to the weak push given to research by the interested customers. Indeed, metal foams have a higher production cost with respect to bulk materials, even the ones with highest performances. On the other hand, metal foams have peculiarities that bulk material cannot reach at all. However, we truly believe that there are many potential applications still not explored for this materials. Indeed, with the increasing worldwide sensitivity for reduction of fuel consumption it can be reasonably supposed that metal foams will find place in many of the tool and facility we commonly face in reality.

Appendix 1: Foam-Tube Interfaces

As previously explained in 2.1, filling tubes with metal foam is a smart solution that brings significant improvements in mechanical properties. In doing this, a relevant role is played by the interface between the tube and the foam. In this study, we discussed the differences in mechanical performances between the natural and the bonded interface tubes. This appendix describes more deeply the characteristics of these interfaces and what happens during foaming.

1.1 Natural (free) interface

The natural interface is the result of the process of foaming already described in 2.2.1 and 2.3.1. This process bring the aluminum to a semisolid state, opening the possibility of the formation of an intermetallic between the two materials in contact. In [21], Monno, Mussi and Negri studied the presence and the morphology of the interlayer between aluminum foam and steel. Precursors, steel tube, and the foaming process were the same described in this study. They found that for air-foamed specimens the intermetallic layer appeared only in a limited zone, probably corresponding to those small areas where there was a real contact. A double layer was observed showing the presence of Fe_2Al_5 near steel and $FeAl_3$ close to the foam. Moreover, during sectioning of the sample, the foam detached from the substrate while the intermetallic layer remained with it (see Figure A 1).

Figure A 1: Sections of foam filled steel tubes and partial detachment of the foam

The weakness of the layer is due to the relatively small time of contact between molten aluminum and steel and to the presence of silicon in both the materials. Indeed, in [22], Yan and Fan underline that silicon strongly reduces the thickness of the intermetallic layer occupying the structural vacancies of the Fe_2Al_5 phase.

As regards the foam filled titanium tubes, no interlayer seems to appear. Yan and Fan [22] remark that the solubility of titanium in aluminum is one order of magnitude lower that the one of steel. This suppresses the growth of the intermediate layer at the interface of solid titanium and molten aluminum. Only about 3 μm thick layer is observed at the solid titanium-liquid aluminum interface, while under the same conditions the intermediate zone of stainless steel is about 30 μm thick. In any case, due to the short time of our foaming process, no adhesion of the foam to the titanium tubes was observed in our specimens. In particular, what keeps the foam inside the tube is a thin burr formed after cutting of the irregular extremities.

1.2 Bonded Interface

In half of the foam-filled titanium tubes studied the aluminum foam is bonded to the tube through the Hysol® 9466™ epoxy glue. The bonding procedure consists of the following steps:

1. First, the foam is extracted from the tube lightly hitting the base of the foam with a soft tip hammer in order to break the burr;
2. Cleaning of the internal surface of the titanium tube with an abrasive paper brush (Figure A 2.a), and then with alcohol and acetone;
3. Manual brushing of the foam's external surface with the brush inclined at 45° (Figure A 2.b) respect to the longitudinal axis and then manual brushing with a steel scourer (Figure A 2.c);
4. Cleaning of the foam cylinder with alcohol and acetone;
5. Drying of the foam and the tube for one night;
6. Application of the adhesive to the tube along the longitudinal axis and uniform application on the surface of the foam (Figure A 3).
7. Insertion of the foam inside the tube and waiting of 48 hours for glue polymerization.

a) *b)* *c)*

Figure A 2: a) cleaning the tube; b) and c) cleaning the foam

a) *b)* *c)*

Figure A 3: a) adhesive Hysol® 9466™; b) application of the adhesive on the tube and in c) on the foam

Hysol® 9466™ is a toughened, industrial grade epoxy adhesive with extended work life. Its shear strength is 26 MPa [23] if applied on abraded aluminum (no data are available for titanium). This value make us truly believe that no detachment between the foam and the tube occurred during bending fatigue test, where the value of maximum axial stress was about 0.038 MPa.

Another type of bonded interface is the one between the APM foam and the steel tube. As already mentioned it 5.2.4, this hybrid APM is made by aluminum foam spheres kept together by an adhesive activated during foaming. This adhesive attaches to the aluminum foam spheres as well as to the internal surface of the steel tube, so that the foam is practically bonded.

Appendix 2: Acoustic Emissions

In physics, sound is a vibration that propagates as a mechanical wave of pressure and displacement, through compressible media such as gases, liquids or solids. As the source continues to vibrate the medium, the vibration propagates away from the source at the speed of sound (depending on the medium itself), thus forming the sound wave.

Acoustic Emission (AE) is a phenomenon in which transient elastic waves are generated by the rapid release of energy from localized sources within a material as it undergoes fatigue. Since plastic deformation and fatigue-crack growth are two principal sources of AE signals, this approach is highly desirable for fatigue assessment [20]. However, AE con be generated from sources not involving the material failure including friction, cavitation or impact.

The AE technique is generally performed using a physical acquisition system as the one described in 4.3.2. The first choice is setting a *threshold* for room noise filtering: commonly 30 dB is a sufficient value of threshold. However, in conditions where noise due to impact or friction can occur, a higher threshold is appropriate: for this reason, we decided to set it to 40 dB. The sensor is a piezoelectric transducer able to give a reasonable response in a frequency range around to its resonance: this is because the pressure level of sound is so weak that a good physical response of the transducer is needed. Figure A 4 show the sensitivity curve of sensor PCA Micro80 utilized in this work.

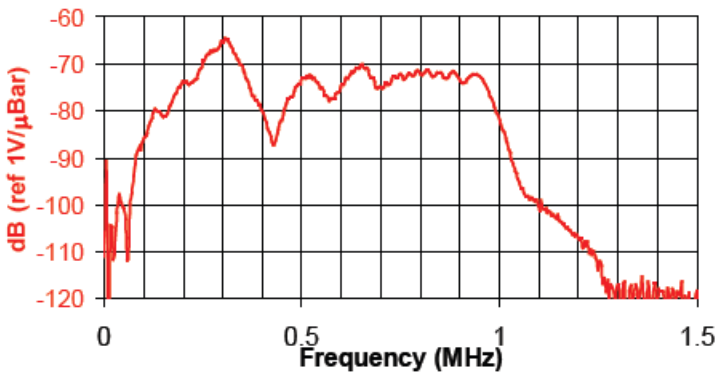

Figure A 4: Sensitivity of Micro80 transducer

Once the signal passes the threshold level the acquisition starts and it continues until the signal goes again under the threshold. After the acquisition, the software computes in real time many parameters of the wave or event happened. The main parameters are amplitude (A), duration (D), rise time (RT) and counts (C): the amplitude is the maximum level reached by the wave; the duration is the time between the first and the last overshoot crossing; the rise time is the time that the wave takes to reach its maximum; the counts are the number of oscillations recorded (see Figure A 5).

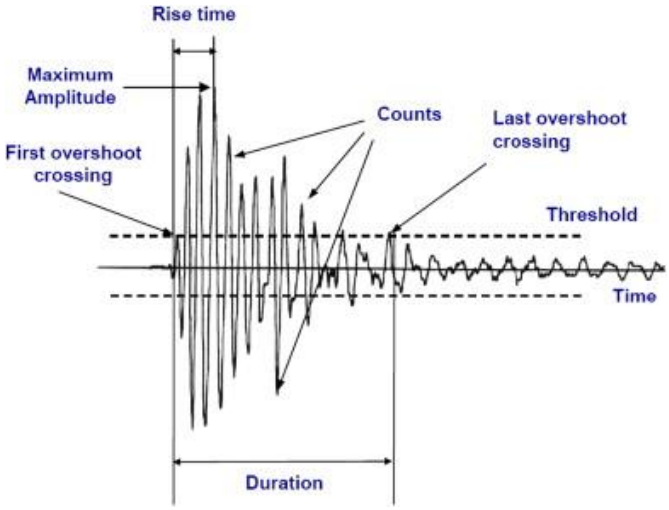

Figure A 5: Hit waveform quantification parameters

Nevertheless, setting only a threshold for noise filtering is not sufficient to identify an event or a wave correctly. The so-called *waveform parameters* are important as well to distinguish an event from noise or undesired data. This is a very crucial and at the same time difficult choice in setting up the acquisition system. These parameters are peak definition time (PDT), hit definition time (HDT), and hit lock-out time (HLT) (see Figure A 6). PDT guarantees the correct recognition of signal peak for rise time measurement. A proper value of the HDT ensures that a single signal hit is recorded as only one hit, determining its end. The HLT closes out the measurement process and stores the hit waveform quantification parameters (amplitude, counts, duration, rise time, and energy) in the data acquisition buffer [20]. Incorrect selection of this values will result in multiple hit data, where two AE hit merge and became one, obviously compromising the quantification parameters.

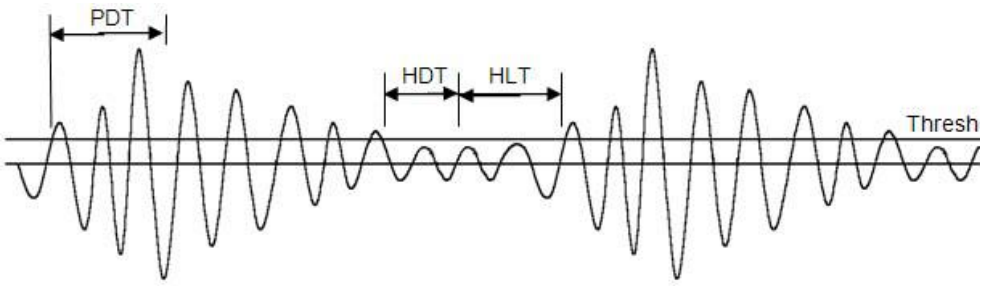

Figure A 6: PDT, HDT, HLT waveform parameters [20]

. In our case, since no experience of this technique was evident in literature for metal foams, we chose to set this parameters according to the manual suggestions for metallic materials (PDT=300 μs, HDT=600 μs, HLT=1000 μs). In any case, for the purposes of this study, this choice was not so crucial. Indeed, we decided to plot parameters that are not strictly sensitive to PDT, HDL, and HLT such as cumulative energy and cumulative counts during the fatigue test, in order to give an idea of the AE activity during cyclic loading. The energy of the signal is the area undergoing the part of the signal that overcomes the threshold, as visible in Figure A 7.

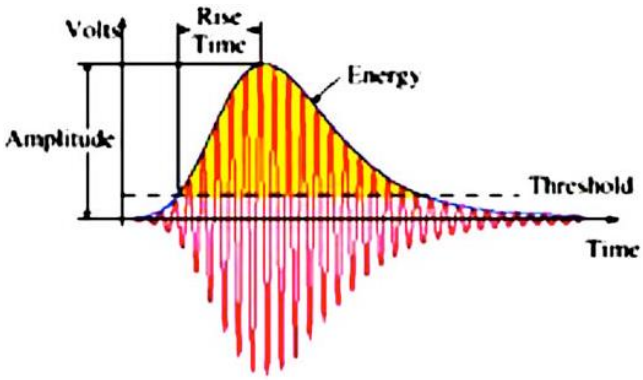

Figure A 7: Energy of the acoustic signal [20]

However, there exist some studies (as [20] on steel and [19] on composite material) focused in separating the different mechanisms of failure inside the material, making use of the wave quantification parameters and with the support of neural networks. It has been found that different mechanism such as plastic deformation, plane stress or plane strain cracks, matrix micro cracking or fiber breaking can be distinguished especially through the amplitude and duration information.

References

[1] J. Banhart, "Light-Metal Foams-History of Innovation and Technological Challenges," *Advanced Engineering Materials,* 2012.

[2] M. F. Ashby, A. G. Evans, N. A. Fleck, L. J. Gibson, J. W. Hutchinson and H. N. Wadley, Metal Foams: A Design Guide, Butterworth Heinemann, 2000.

[3] C. J. Yu, H. H. Eifert, J. Banhart and J. Baumeiser, "Metal foaming by a powder metallurgy method: Production, properties and applications," *Springer-Verlag,* 1998.

[4] A. Villa, «Produzione di barre tubolari anti-intrusione laterali tramite schiumatura metallica,» Politecnico di Milano, 2010.

[5] J. Banhart, "Manufacture, characterisation and application of cellular metals and metal foams," *Progress in Material Science,* 2010.

[6] I. Golovin and H.-R. Sinning, "Interal friction in metallic foams and some related cellular structures," *Material Science & Engineering,* 2004.

[7] J. Banhart, J. Baumeister and M. Weber, "Damping properties of aluminum foams," *Material Science & Engineering,* 1996.

[8] F. Han, Z. Zhu, C. Liu and J. Gao, "Damping behavior of foamed aluminum," *Metallurgical and Material Transaction A,* vol. 30A, 1999.

[9] I. Golovin, H.-R. Sinning, J. Göken and W. Rieheman, "Fatigue-related damping in some cellular metallic materials," *Material Science & Engineering,* 2004.

[10] "http://live.pege.org/2005-material/kohlefasern-mit-stahl-hohlkugeln.htm," [Online].

[11] "http://www.popularmechanics.com/," 28 April 2012. [Online].

[12] V. C. Srivastava and K. L. Sahoo, "Processing, stabilization and applications of metallic foams. Art of science," *Materials Science-Poland,* 2007.

[13] "http://www.instron.it/," [Online].

[14] "http://www.selee.com/Selee_Corporation_Metal_Foam.php," [Online].

[15] "http://www.ifam.fraunhofer.de/," [Online]. Available: http://www.ifam.fraunhofer.de/en/Dresden/Energy_and_thermal_management/leistungen_und_methoden.html.

[16] H. Zarei and M. Kröger, "Bending behavior of empty and foam-filled beams: Structural optimization," *International Journal of Impact Engineering,* 2008.

[17] ASM Aerospace Specification Metals Inc., "http://asm.matweb.com/," [Online].

[18] A. Belfiglio, "Mechanical performance of metal tubes filled with metal foams:prototype parts for machine tools and helicopters," Politecnico di Milano, 2013.

[19] A. Bravo, T. Lotfi, K. Demagna and E. Fouad, "Characterization of tensile damage for a Short Birch Fiber-Reinforced Polyethylene Composite with Acoustic Emission," *International Journal of Material Science,* vol. 3, 2013.

[20] F. F. Barsoum, J. Suleman, A. Korcak and E. V. K. Hil, "Acoustic emission monitoring and fatigue life prediction in axially loaded notched steel specimens," *Journal of Acoustic Emission,* no. 29, 2009.

[21] M. Monno, V. Mussi and D. Negri, "Aluminium foam/steel interface formed during foaming process in air or argon flow: a micro structural comparison.".

[22] M. Yan and Z. Fan, "Durability of materials in molten aluminum alloys," *Journal of Material Science,* 2001.

[23] "Hysol 9466™- Technical Data Sheet," Loctite, 2006.

[24] C. Kammer, "Aluminium Foam," Talat, Goslar, Germany, 1999.

[25] T. Lyman, Metals Handbook Vol. 8: Metallography, Structures and Phase, 1973.

[26] C. J. Yu and J. Banhart, "Mechanical Properties of Metallic Foams".

[27] C. Kádára, F. Chmelik, Z. Rajkovits and J. Lendvai, "Acoustic emission measurements on metal foams," *Journal of Alloys and Compounds*, 2004.

[28] G. Diana and F. Cheli, Dinamica dei sistemi meccanici, Milano: Polipress, 2010.

[29] J. Yu, X. Wang, Z. Wei and E. Wang, "Deformation and failure mechanism of dynamically loaded sandwich beams with aluminum-foam core," *International Journal of Impact Engineering*, 2003.

[30] V. Dattoma, N. Giannoccaro, A. Messina and R. Nobile, "Fatigue damage evaluation of metallic foam specimens through modal data," in *Proceedings of the XIth International Congress and Exposition*, Orlando, Florida, USA, 2008.